Solar Phys (2015) 290:437–466
DOI 10.1007/s11207-014-0629-0

A Minimum Energy Fit Method to Reconstruct Photospheric Velocity and Magnetic Diffusivity in Active Regions from Observed Magnetograms and Dopplergrams

Benoit Tremblay · Alain Vincent

Received: 9 November 2013 / Accepted: 10 November 2014 / Published online: 12 December 2014

Abstract We introduce MEF-R, a generalization of the minimum energy fit (MEF; Longcope, *Astrophys. J.* **612**, 1181, 2004) to a non-ideal (resistive) gas. The new technique requires both vector magnetograms and Doppler velocities as input fields. However, in the case of active regions observed only with the *Michelson–Doppler Imager* (MDI) onboard the *Solar and Heliospheric Observatory* (SOHO) such as AR 9077, we have only access to line-of-sight magnetograms. We reconstruct two-dimensional maps of the magnetic diffusivity $\eta(x, y)$ together with velocity components $v_x(x, y)$, $v_y(x, y)$, and $v_z(x, y)$ under the linear force-free magnetic field approximation. Computed maps for $v_z(x, y)$ very well match the Doppler velocities $v_r(x, y)$. We find the average value $\langle\eta\rangle \approx 10^8\ \mathrm{m^2\,s^{-1}}$ with a standard deviation of $\approx 10^{10}\ \mathrm{m^2\,s^{-1}}$. Such high values of $\eta(x, y)$ are to be expected at some places since our magnetic diffusivity is actually eddy-diffusivity. Inside AR 9077, the maps of $\eta(x, y)$ do not resemble closely the maps from classical models of the magnetic diffusivity, but they are closer to η as a function of temperature than to η as a function of electric current density.

Keywords Eddy-diffusivity · Magnetograms · Minimum energy fit · Photosphere · Velocity fields

1. Introduction

Observations and numerical simulations show that in solar active regions, flares are often preceded by emerging sunspots (Ilonidis, Zhao, and Kosovichev, 2011) under the form of vertical plasma motions (Bellot Rubio *et al.*, 2001; Harra *et al.*, 2012).

Various techniques have been proposed to reconstruct velocity vectors from any consecutive set of line-of-sight or vector magnetograms. The frozen-in-flux theorem (Alfvén,

---

B. Tremblay · A. Vincent (✉)
Département de Physique, Université de Montréal, C.P. 6128, Succ. A, Montréal, Québec H3C 3J7, Canada
e-mail: vincent@astro.umontreal.ca

1942) is valid for a perfectly conducting fluid with no magnetic resistivity. Magnetic induction $\boldsymbol{B}$ is frozen-in to the plasma and passively follows plasma motions $\boldsymbol{v}$. To this date and although it could have been theoretically possible, none of these techniques have been used for resistive plasmas. Local correlation tracking (LCT) would work best if the line-of-sight magnetic field $\boldsymbol{B}_\ell$ is advected in a velocity field with a constant profile. However, such a field being not necessarily a solution of the magnetic induction equation, LCT alone has been shown to be inconsistent with the equation of magnetic induction (Schuck, 2005). The method of inductive local correlation tracking (ILCT; Welsch *et al.*, 2004; Schuck, 2005) combines both. If vector magnetograms computed from the Stokes polarimetry are used, the minimum structure reconstruction (MSR; Georgoulis and LaBonte, 2005) addresses the 180° azimuth ambiguity (*e.g.* Metcalf *et al.*, 2006) but does not work in the case of rapidly varying local magnetic fluxes such as an emergence or submergence. As far as the motions are restricted to horizontal directions, techniques using line-of-sight magnetograms are known to work, but to reconstruct vertical velocities vector magnetograms should be used (Schuck, 2008). The differential affine velocity estimator (DAVE) for vector magnetograms (Schuck, 2008) finds a two-dimensional affine profile for all three components of the photospheric velocity but does not need Doppler velocities. The minimum energy fit (MEF; Longcope, 2004) with a reference background velocity v_r (which could possibly be taken from the Doppler velocity) is a self-consistent method that gives a unique vector velocity field solution to the ideal magnetic induction equation. Due to the stabilizing effect of strong magnetic fields, it is reasonable to have the total kinetic energy minimal in active regions except during flares or during the emergence of an active region. A poloidal–toroidal decomposition (PTD) of the magnetic field (Fisher *et al.*, 2010) includes Doppler velocity observations. Doppler velocities have to be taken into account as a constraint to compute accurate electric fields and Poynting fluxes (Fisher, Welsch, and Abbet, 2012b). Hybrid techniques are also proposed. A combination of MEF, LCT, and Doppler velocity is best to reconstruct $\boldsymbol{v}$ and this is shown by using anelastic MHD (ANMHD; Fan *et al.*, 1999) test flows (Ravindra, Longcope, and Abbett, 2008). FLCT and DAVE (Welsch *et al.*, 2009) can be used to study photospheric flows and deduce energy fluxes to be compared with soft X-ray flux data. ILCT and MEF (Santos, Büchner, and Zhang, 2008) have been used to compute emerging/submerging flow as well as horizontal motions.

To test any algorithm, analytical solutions are useful but are very difficult to find. Therefore, specific output data from numerical simulations of convection have been used instead. For instance ANMHD (Fan *et al.*, 1999) was used to compute solar-like anelastic convection (Lantz and Fan, 1999) but without the complexity of the photosphere. Most of the above techniques were compared (Welsch *et al.*, 2007) and have shown a performance comparable to (but slightly lower overall than) MEF. It was found generally difficult to reconstruct v_z from v_r (Georgoulis and LaBonte, 2005). A method like MEF (Longcope, 2004) may compute v_z, if it has some similarities with v_r, starting from $B_{x,y,z}(t)$ and $B_{x,y,z}(t+\mathrm{d}t)$ only if v_r is taken as a background vertical reference velocity.

To reconstruct a velocity field, MEF needs sequences of vector magnetograms. Such measurements are now made at regular time intervals and high resolution by ground-based observatories (*e.g.* the Vector Spectromagnetograph (VSM) from the *Synoptic Optical Long-term Investigations of the Sun* (SOLIS; Keller *et al.*, 2001) or the Near InfraRed Imaging Spectropolarimeter (NIRIS; Cao *et al.*, 2012) of the *New Solar Telescope* (NST) of the Big Bear Solar Observatory (BBSO) and by instruments like the Spectro-Polarimeter of the *Solar Optical Telescope* onboard *Hinode* (Kosugi *et al.*, 2007) or the *Helioseismic and Magnetic Imager* (HMI; Schou *et al.*, 2012) onboard the *Solar Dynamics Observatory* (SDO).

However, in this study of AR 9077, we used the line-of-sight magnetograms B_ℓ from the *Michelson–Doppler Imager* (MDI; Scherrer *et al.*, 1995) onboard *Solar and Heliospheric*

Observatory (SOHO). In this case, the only way B_x, B_y, and B_z can be reconstructed from B_ℓ alone is to use the force-free (FF) assumption.

The photosphere is a dynamic medium (DeRosa *et al.*, 2009) and there is an interaction between the Lorentz force in the lower corona and the magnetic field in the photosphere and especially during flares (Fisher *et al.*, 2012a). Nevertheless, except during the emergence of an active region or during a flare, the magnetic field of the photosphere has been approximated as force-free (Moon *et al.*, 2002; Tiwari, 2011) but this may be only true at 400 km above the photosphere (Metcalf *et al.*, 1995) or inside sunspots where the magnetic field is the strongest (Tiwari, 2011). In this study, we have used the linear force-free approximation (LFF; Nakagawa and Raadu, 1972), with the twist α as a free parameter taken from the literature (*e.g.* Régnier and Priest, 2007). Geometrical distortion due to sphericity of the solar surface is a problem if the active region under study is located too far from the center of the solar disk. But even if corrected (*e.g.* Welsch *et al.*, 2009), part of the real value of B_z has been lost in the projection.

There are several mechanisms to explain why the reconstructed v_z is not v_r. Here we suppose that the magnetic field is not completely frozen-in to the plasma and that there must exist an eddy magnetic diffusivity inside the photosphere and the chromosphere that would be due to small scale fluctuations of unresolved current, temperature, or velocity. Indeed, theoretical magnetic diffusivities (Ohmic, Hall, and ambipolar) in the photosphere and chromosphere are in the range of $\eta \approx [10^3, 10^6]\ \mathrm{m^2\,s^{-1}}$ (*e.g.* Singh *et al.*, 2011; Pandey and Wardle, 2012, 2013) or even higher $\eta_\mathrm{O} \approx 10^8\ \mathrm{m^2\,s^{-1}}$ (Abramenko *et al.*, 2011; Cameron, Vögler, and Schüssler, 2011) but are pixel-size dependent (Chae, Litvinenko, and Sakurai, 2008). Such high values are explained as turbulent or eddy magnetic diffusivity (*e.g.* Chae, Litvinenko, and Sakurai, 2008) with a smallest resolved scale (the subgrid) as large as a solar granule (Simon and Weiss, 1997). Higher values of the magnetic diffusivity would locally produce stronger Joule heating (Spangler, 2009). Reconnection of the magnetic field lines may occur not only in the corona but also in the chromosphere (Heggland, De Pontieu, and Hansteen, 2009). This can be modeled by a critical value of the electric current of $J_\mathrm{c} \approx 1.4 \times 10^{-3}\ \mathrm{A\,m^{-2}}$ (Büchner, Nikutowski, and Otto, 2004), above which the magnetic resistivity would sharply increase. In this case, η_eddy is due to small scale current instabilities (Lu, 1995; Klimas *et al.*, 2004; Uritsky and Klimas, 2005).

The purpose of this study is to reconstruct (v_x, v_y, v_z) from (B_x, B_y, B_z) computed from B_ℓ observed with SOHO/MDI under the assumption of the force-free condition and using the resistive magnetic induction equation. Anomalous diffusivity η_eddy would be adjusted locally so that v_z be as close as possible to the observed Doppler velocity v_r while v_x and v_y be such that the total kinetic energy is minimal. In this sense, our method could be labeled as a “Doppler-diffusivity matching” (DDM) technique. We have applied the new MEF with resistivity (MEF-R method) to SOHO/MDI observations of AR 9077 on 14 July 2000 having produced the X5.7 GOES X-ray class “Bastille” Day flare. It has been extensively studied in the literature (see the Topical Issue, *Solar Physics* **204**, 2001). A detailed study of horizontal motions has shown that AR 9077 was in a highly sheared state and that the initiation of the two-ribbon flare followed an episode of flux emergence (Liu and Zhang, 2001; Somov, 2007). The motion of the flare propagation together with the dynamics of this two-ribbon system is best seen at 171 Å from TRACE (*Transition Region and Coronal Explorer*) data (Aschwanden, 2008).

The manuscript is organized as follows. In Section 2 we explain in detail the processing of the data. In Section 3, we show that MEF alone does not produce vertical velocities matching the observed Doppler velocities. In Section 4, we derive MEF-R, a generalization of MEF to resistive plasmas. We start from the resistive induction equation and use the force-free

Table 1 AR 9077 on 14 July 2000. Times (UT) are given at which we computed $\boldsymbol{v}$ from B_ℓ magnetograms recorded by SOHO/MDI and Imaging Vector Magnetograph at Mees Observatory at Haleakala (16:33 UT).

Time (UT)	Time interval dt (s)	Comment
00:00 – 01:39	5940	Start simulation
01:39 – 03:15	5760	
03:15 – 04:51	5760	
04:51 – 06:24	5580	
06:24 – 08:00	5760	
08:00 – 09:36	5760	
09:36 – 10:30	3240	
10:30 – 11:12	2520	Flare from 10:30 to 10:50 UT
11:12 – 12:48	5760	Thermalization phase
12:48 – 16:33	13500	
16:33 – 20:48	15300	
20:48 – 01:36	17280	End simulation

condition. In Section 5, we use MEF-R to study AR 9077 using SOHO/MDI magnetograms and Dopplergrams. We discuss vertical velocity versus Doppler velocity, horizontal velocity vector maps, and the meaning of the magnetic eddy diffusivity. In Section 6, we show that the time evolution of Doppler velocity, magnetic diffusivity, and Poynting energy flux can predict the flare. Finally, in the conclusion (Section 7), we discuss open questions and work under way.

2. Data Preprocessing: AR 9077

To test MEF-R, we processed active region AR 9077. It has produced the "Bastille Day" flare on 14 July 2000, an X5.7 GOES X-ray class flare that has been studied by several authors (*e.g.* Chertok and Grechnev, 2005; Aschwanden, 2008).

We used moderate resolution (≈ 1.98 arcsec per pixel) line-of-sight full-disk magnetograms $B_\ell(t; t+\mathrm{d}t)$ and Dopplergrams $v_r(t; t+\mathrm{d}t)$ recorded with SOHO/MDI (Table 1). The difficulty and the need of a complex processing have been emphasized by numerous authors in the past. There are several processing steps to do. First, we extracted a square domain of area ($386 \times 386\ \mathrm{Mm}^2$) around the sunspot of maximal lifespan. Second, we removed the bad pixels (*e.g.* X-ray or proton hits on the CCD). Third, we applied a local smoothing over 3×3 points whenever necessary (bad pixels or missing data) (*e.g.* Fuhrmann *et al.*, 2011). Spherical distortion and projection effects have not been considered because AR 9077 was at latitude 17°N and close enough to disk center at the times we consider. We choose to crudely approximate photospheric fields as force-free (*e.g.* Moon *et al.*, 2002; Seehafer *et al.*, 2007; Tiwari, 2011). Thus, vector magnetograms can be reconstructed from the line-of-sight SOHO/MDI magnetograms B_ℓ, which we assumed to be equal to B_z. We computed vector magnetograms (B_x, B_y, B_z) from $B_z \approx B_\ell$ using a spectral Fourier–Laguerre technique based on the linear force-free assumption (Nakagawa and Raadu, 1972) in which $\alpha^2 = (k_x^2 + k_y^2 - k_z^2)$ with $k_x = 2\pi/L_x$, $k_y = 2\pi/L_y$, and $k_z = \pi/L_z$. The value of α was chosen such that $\alpha = \langle \boldsymbol{B} \cdot \nabla \times \boldsymbol{B}\rangle / \langle \boldsymbol{B} \cdot \boldsymbol{B}\rangle$ ($\langle\ \rangle$ represents the spatial average). The required mean value of the local twist (*e.g.* Hao and Zhang, 2011) is taken as constant over the entire active region. We set for the entire time sequence $\alpha \approx -1.5 \times 10^{-2}\ \mathrm{Mm}^{-1}$, a realistic value (*e.g.* Sakurai and Hagino, 2003;

Régnier and Priest, 2007). The components $B_x(x,y)$ and $B_y(x,y)$ of the horizontal magnetic field $\boldsymbol{B}_h$ are shown in Figure 1. The resulting vector magnetogram (B_x, B_y, B_z) is a force-free and divergence-free field with $\nabla\cdot\boldsymbol{B}/\langle(\frac{\partial B_x}{\partial x})^2+(\frac{\partial B_y}{\partial y})^2+(\frac{\partial B_z}{\partial z})^2\rangle^{1/2}\leqslant 10^{-7}$ as in Contopoulos, Kalapotharakos, and Georgoulis (2011). For all three components, the polarity inversion lines can be seen near the center of the map (Figure 1).

The Doppler velocities v_r are also from SOHO/MDI data archives and were extracted over the same area on the solar disk. Because MDI uses the same Ni I 6768 Å line, both Dopplergrams and magnetograms are observed at the same optical depth, very close to the standard 5000 Å defining the altitude of the photosphere (*e.g.* Steffen, 2009). The motion of the observer, the limb shift, as well as the Sun's rotation have been removed using 'standard' models (Snodgrass, 1984; Snodgrass and Ulrich, 1990). But we did not process the data as completely as in Schuck (2010). In particular, the p-mode oscillations have not been removed. The p-modes could produce velocities up to a few hundred meters per second (*e.g.* Hathaway *et al.*, 2000). Furthermore, Dopplergrams were only available at 12:00 and 16:54 UT on 13 July 2000, 00:16, 06:11 and 10:30 UT on 14 July 2000 and 05:05 and 11:20 UT on 15 July 2000. A second-order time interpolation has been used to produce Dopplergrams at the same times as available magnetograms (see Table 1).

The resulting maps have a grid size of 256 × 256 pixels corresponding to an area of about $500\times 500\ \text{arcsec}^2$ or $386\times 386\ \text{Mm}^2$ on the solar disk.

3. MEF Technique for Ideal MHD Alone

To compute photospheric velocities, MEF (Longcope, 2004) needs sets of vector magnetograms (B_x, B_y, B_z) taken at two consecutive times $(t; t+\mathrm{d}t)$. In the case of AR 9077, we had no access to time sequences of vector magnetograms. Also, as explained below (Section 4.1), we did not have enough information to compute the vertical derivatives of $\boldsymbol{B}$. Thus, although MEF would be valid for any magnetic field, we had to use the force-free approximation $\mu_0\boldsymbol{J}=\alpha\boldsymbol{B}$.

In this study, we have used the IDL version of MEF available at http://solar.physics.montana.edu/dana/. To avoid divisions by zero during the computations using MEF, $|B_z|\geqslant 1$ gauss (G) has been imposed locally as a minimum value except in the computations of $1/|B_z|$ where we impose $|B_z|\geqslant 40$ G. This empirical value has been set above the noise (≈20 G) in our data. At the 11 times listed in Table 1, we computed velocities $\boldsymbol{v}$ and compared $v_z(t)$ with the Doppler velocity $v_r(t)$ observed with SOHO/MDI. We found that without any reference velocity field $\boldsymbol{u}=\boldsymbol{0}$, $v_z(t)$ is very different from $v_r(t)$ (not shown). Even when using $v_r(t)$ as a background vertical velocity we find differences. As an example, using MEF and 1000 iterations, we computed the vertical velocity v_z between 08:00 and 09:36 UT, just before the flare. At this time, both Doppler and Zeeman shifts are still reliable. The vector magnetogram (B_x, B_y, B_z) is shown as an average between 08:00 and 09:36 UT in Figure 1 and the corresponding Doppler velocity v_r is displayed in Figure 2(a). Although the minima are located at the right places, there are significant differences between v_r and MEF-computed v_z (Figure 2(b)). The differences are quantified by a scatter plot (Figure 2(c)). A quantitative global estimate of how close are two two-dimensional (2D) spatial distributions $A(x,y)$ and $B(x,y)$ is given by their correlation coefficient: $C(A,B)=(\Sigma_{x,y}A\cdot B)/(\Sigma_{x,y}A^2\cdot\Sigma_{x,y}B^2)^{1/2}$. We found that $C(v_r,v_z)\approx 0.906$ for $1\ \text{G}\leqslant|B_\ell|\leqslant 2500$ G. If we separate a weak field contribution we obtain $C(v_r,v_z)\approx 0.909$ for $1\ \text{G}\leqslant|B_\ell|\leqslant 200$ G. Likewise if we separate a strong-field contribution we obtain $C(v_r,v_z)\approx 0.805$ for $500\ \text{G}\leqslant|B_\ell|\leqslant 2500$ G. The high values of correlation coefficients

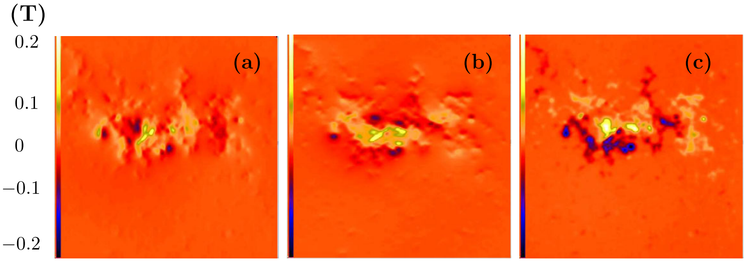

Figure 1 Vector magnetograms (a) $B_x(x, y)$, (b) $B_y(x, y)$, and (c) $B_z(x, y) \equiv B_\ell(x, y)$ of AR 9077 on 14 July 2000. The magnetograms (a) and (b) were reconstructed from the line-of-sight magnetograms (c) recorded by SOHO/MDI by using the linear force-free hypothesis (Nakagawa and Raadu, 1972) with $\alpha \approx -1.5 \times 10^{-2}\ \mathrm{Mm}^{-1}$ (Régnier and Priest, 2007). $\boldsymbol{B}$ has been averaged between 08:00 and 09:36 UT and smoothed with a 3 × 3 pixels spatial filter. The grid size is 256 × 256 pixels. The area covered is about 500 × 500 arcsec^2. The color scales range from −0.2 T to 0.2 T.

Figure 2 (a) Doppler velocity $v_r(t)$ in AR 9077 recorded by SOHO/MDI on 14 July 2000. The Sun's rotation has been removed. (b) $v_z(t)$ as computed using MEF with $v_r(t)$ as a background vertical velocity. The time interval is 08:00 – 09:36 UT and the grid size is 256 × 256 pixels in both panels. Panel (c) shows the scatter plot between $v_z(t)$ and $v_r(t)$.

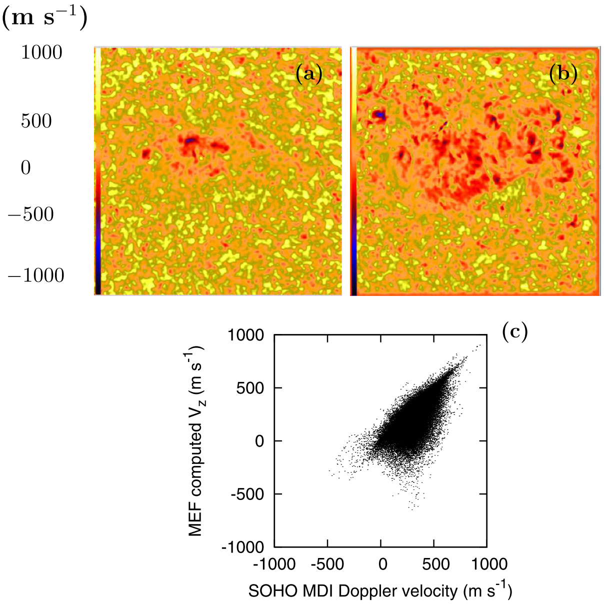

here are mostly due to the global minimization process of MEF and do not reflect local differences. As noted by Ravindra, Longcope, and Abbett (2008), Doppler velocity observations alone could conflict with the conservation of magnetic flux. We have made the hypothesis that these differences are due to the fact that the magnetic field is not simply frozen-in to the plasma and have generalized MEF to include a magnetic diffusivity (MEF-R). Due to the size of a pixel in our data (see below, 1 pixel ≈ 1500 km), one cannot expect η to be a collisional diffusivity but a turbulent or eddy diffusivity.

4. MEF-R: A Generalization of the MEF Technique to Resistive Plasmas

In the following, we locate the photosphere at the origin of the vertical coordinate $z = 0$ in Cartesian geometry. Each vector quantity observed or computed at the photospheric level has a vertical component, normal to the photospheric plane, subscripted with "z" and a horizontal component subscripted with "h".

4.1. Resistive Induction Equation

The non-ideal or resistive induction equation is used here to describe the behavior of the photospheric magnetic field $\boldsymbol{B}$ and its time evolution

$$\begin{aligned}\frac{\partial \boldsymbol{B}}{\partial t} &= \nabla \times \bigl[(\boldsymbol{v} \times \boldsymbol{B}) - \eta(\nabla \times \boldsymbol{B})\bigr] \\ &= \nabla \times \bigl[(\boldsymbol{v} \times \boldsymbol{B}) - \eta\mu_0 \boldsymbol{J}\bigr],\end{aligned} \tag{1}$$

where $\eta = \eta(x, y; t)$ is the magnetic diffusivity and is a function of space and time,

$$\eta(x, y) = \frac{1}{\mu_0 \sigma}, \tag{2}$$

σ being the conductivity. A consistent velocity flow can be derived, as in the case of non-resistive ideal MHD, by considering the vertical component of the non-ideal equation of magnetic induction (Equation (1))

$$\begin{aligned}\frac{\partial B_z}{\partial t} &= \bigl[\nabla \times (\boldsymbol{v} \times \boldsymbol{B})\bigr]_z - (\nabla \times \eta\mu_0 \boldsymbol{J})_z \\ &= \nabla_h \cdot \bigl[(v_z \boldsymbol{B}_h - B_z \boldsymbol{v}_h) + \eta(\hat{\boldsymbol{z}} \times \mu_0 \boldsymbol{J}_h)\bigr].\end{aligned} \tag{3}$$

Here we suppose that the discrepancies between v_z as computed by MEF and Doppler velocity v_r observed by SOHO/MDI are due to the fact that the magnetic field is not frozen-in to the plasma flow but there is also a magnetic diffusivity $\eta(x, y)$. This may be only partially true since we did not have access to the vertical derivatives of the magnetic field outside of the FF assumption, but $\eta(x, y)$ would not be a collisional magnetic diffusivity.

As noticed by Longcope (2004), it would be impossible to solve the resistive induction equation in a single plane. Indeed, the second term on the right-hand side of Equation (3) includes vertical spatial derivatives of first order for $\boldsymbol{B}_h$. In order to approximate these derivatives, one must rely on data from at least two planes at different vertical heights at and above the photosphere, all at the same time t_j. Quantities such as J_x and J_y, or simply $\boldsymbol{J}_h$, could be computed since we suppose that the magnetic field at the photospheric level is a force-free field.

4.2. Unknown Scalar Potentials

Helmholtz's theorem allows for a differentiable vector function going to zero fast enough as r goes to infinity to be expressed as the sum of the gradient of a scalar function and the curl of a potential vector (*e.g.* Griffiths, 2007). This approach was used by Longcope (2004) to rewrite Equation (3) in terms of two scalar potentials ϕ and ψ for an ideal MHD ($\eta = 0$). Here we use Helmholtz's theorem to decompose a vector function including a resistive term,

$$\boldsymbol{F} = (v_z \boldsymbol{B}_h - B_z \boldsymbol{v}_h) + \eta(\hat{\boldsymbol{z}} \times \mu_0 \boldsymbol{J}_h). \tag{4}$$

The magnetic fields considered in this study are not bounded and could not be so, even locally, because they are force-free (Brownstein, 1994). However, as mentioned above, Helmholtz's theorem does not require a bounded domain to be valid. In the general case of $\alpha = \alpha(x, y) = \mu_0 J_z / B_z$, the differentiability of the vector function $\boldsymbol{F}$ is not always satisfied if $\eta \neq 0$ as its second term in Equation (4), $\eta(\hat{z} \times \mu_0 \boldsymbol{J}_h)$, cannot be differentiated where B_z is 0. The problem arises from the force-free approximation of $\boldsymbol{B}$ as the horizontal current density $\boldsymbol{J}_h$ depends on the inverse of B_z. As in the case of MEF (Section 3), we used a threshold so that $|B_z| \geqslant 40$ G everywhere on the photospheric plane. Thus, with every condition satisfied, applying Helmholtz's theorem to the vector function in Equation (3) yields

$$\boldsymbol{F} = (v_z \boldsymbol{B}_h - B_z \boldsymbol{v}_h) + \eta(\hat{z} \times \mu_0 \boldsymbol{J}_h) = \nabla_h \phi + \nabla_h \times \psi \,\hat{\boldsymbol{z}} = \nabla_h \phi + \nabla_h \psi \times \hat{z}. \tag{5}$$

The formalism introduced in Equation (5) leads to the same result for both resistive and ideal forms of the induction equation as we rewrite Equation (3) in terms of ϕ and ψ, *i.e.* a Poisson equation for ϕ,

$$\begin{aligned} \frac{\partial B_z}{\partial t} &= \nabla_h \cdot (\nabla_h \phi + \nabla_h \psi \times \hat{z}) \\ &= \nabla_h^2 \phi. \end{aligned} \tag{6}$$

Mathematically, ϕ has the form of the electrostatic potential arising from a charge distribution given by $\frac{\partial B_z}{\partial t}$ whereas ψ is a potential function generating the solenoidal part of the electric field (Longcope, 2004). The same method can therefore be applied to the solution of Equation (6) for ϕ, *i.e.* reversing the Laplacian operator and using $\phi = 0$ as a boundary condition for all points that are not in the active region interior (Longcope, 2004) or, in our study, at the border of the computational domain.

4.3. The Minimum Energy Fit

By rearranging the terms in Equation (5), the horizontal velocity $\boldsymbol{v}_h$ can be written as a function of ϕ, ψ, v_z, and η,

$$\boldsymbol{v}_h = \frac{[v_z \boldsymbol{B}_h - \nabla_h \phi - \nabla_h \psi \times \hat{z} + \eta(\hat{z} \times \mu_0 \boldsymbol{J}_h)]}{B_z}. \tag{7}$$

There are an infinite number of solutions for $\boldsymbol{v}_h$ as the formalism introduced in Equation (5) results in the resistive induction equation being satisfied regardless of the field ψ. As for ideal MHD, the minimization of a penalty function guarantees a unique solution for $\boldsymbol{v}_h$. It is expected that inside an active region where the magnetic fields are strong the total kinetic energy would be reduced. Thus, we use the same energy-like functional W previously introduced for the MEF, the only difference being that it is also a function of a third field, $\eta(x, y)$, as a result of Equation (7)

$$\begin{aligned} W \equiv W\{\psi, v_z, \eta\} &= \int_M L\left\{x, y, \psi, \frac{\partial \psi}{\partial x}, \frac{\partial \psi}{\partial y}, v_z, \frac{\partial v_z}{\partial x}, \frac{\partial v_z}{\partial y}, \eta, \frac{\partial \eta}{\partial x}, \frac{\partial \eta}{\partial y}\right\} \mathrm{d}x\, \mathrm{d}y \\ &= \frac{1}{2} \int_M |\boldsymbol{v}_h - \boldsymbol{u}_h|^2 + |v_z - u_z|^2 \,\mathrm{d}x\, \mathrm{d}y \\ &\quad + \lambda \int_M \left| \nabla_h \left(\eta \frac{|\mu_0 \boldsymbol{J}|}{B_z} \right) \right|^2 \mathrm{d}x\, \mathrm{d}y, \end{aligned} \tag{8}$$

where M is a region of the photosphere and $\boldsymbol{u}_h$ and u_z are the components of the reference flow $\boldsymbol{u}$ that $\boldsymbol{v}$ tries to fit. For example, Doppler velocity could be used as a reference vertical velocity u_z. This possibly ill-posed problem is treated in MEF-R with a Tikhonov regularization (Tikhonov, 1963) that maximizes correlation between neighboring points (x, y). Here λ is a Lagrange multiplier set to 0.4 px^2 in the case of the Spheromak (Section 4.5).

Minimization of the functional W in terms of ψ, v_z, and η is made using a set of three Euler–Lagrange equations involving the Lagrangian L,

$$\frac{\partial L}{\partial v_z} - \frac{\mathrm{d}\frac{\partial L}{\partial v_{zx}}}{\mathrm{d}x} - \frac{\mathrm{d}\frac{\partial L}{\partial v_{zy}}}{\mathrm{d}y} = 0, \tag{9}$$

$$\frac{\partial L}{\partial \psi} - \frac{\mathrm{d}\frac{\partial L}{\partial \psi_x}}{\mathrm{d}x} - \frac{\mathrm{d}\frac{\partial L}{\partial \psi_y}}{\mathrm{d}y} = 0, \tag{10}$$

$$\frac{\partial L}{\partial \eta} - \frac{\mathrm{d}\frac{\partial L}{\partial \eta_x}}{\mathrm{d}x} - \frac{\mathrm{d}\frac{\partial L}{\partial \eta_y}}{\mathrm{d}y} = 0, \tag{11}$$

where we set $v_{zx} \equiv \frac{\partial v_z}{\partial x}$, $v_{zy} \equiv \frac{\partial v_z}{\partial y}$, $\psi_x \equiv \frac{\partial \psi}{\partial x}$, $\psi_y \equiv \frac{\partial \psi}{\partial y}$, $\eta_x \equiv \frac{\partial \eta}{\partial x}$, $\eta_y \equiv \frac{\partial \eta}{\partial y}$. Since $\frac{\partial L}{\partial \psi} = \frac{\partial L}{\partial v_{zx}} = \frac{\partial L}{\partial v_{zy}} = \frac{\partial L}{\partial \eta_x} = \frac{\partial L}{\partial \eta_y} = 0$, the above equations can be reduced to

$$\frac{\partial L}{\partial v_z} = \frac{\boldsymbol{B}_h \cdot (\boldsymbol{v}_h - \boldsymbol{u}_h)}{B_z} + (v_z - u_z) = 0, \tag{12}$$

$$-\frac{\mathrm{d}\frac{\partial L}{\partial \psi_x}}{\mathrm{d}x} - \frac{\mathrm{d}\frac{\partial L}{\partial \psi_y}}{\mathrm{d}y} = \nabla_h \cdot \left[\frac{\hat{\boldsymbol{z}}}{B_z} \times (\boldsymbol{v}_h - \boldsymbol{u}_h)\right] = 0, \tag{13}$$

$$\frac{\partial L}{\partial \eta} = \frac{(\hat{\boldsymbol{z}} \times \mu_0 \boldsymbol{J}_h) \cdot (\boldsymbol{v}_h - \boldsymbol{u}_h)}{B_z} = 0. \tag{14}$$

With the use of vector identities, one finds that ψ, v_z, and η must satisfy the following three coupled Euler–Lagrange equations:

$$v_z = \frac{B_z^2\, u_z + \boldsymbol{B}_h \cdot [\nabla_h \phi + \nabla_h \psi \times \hat{\boldsymbol{z}} + B_z \boldsymbol{u}_h - \eta(\hat{\boldsymbol{z}} \times \mu_0 \boldsymbol{J}_h)]}{|\boldsymbol{B}|^2}, \tag{15}$$

$$\nabla_h \cdot \left(\frac{\nabla_h \psi}{B_z^2}\right) = \nabla_h \cdot \left[\frac{\hat{\boldsymbol{z}} \times (v_z \boldsymbol{B}_h - \nabla_h \phi - B_z \boldsymbol{u}_h + \eta(\hat{\boldsymbol{z}} \times \mu_0 \boldsymbol{J}_h))}{B_z^2}\right], \tag{16}$$

$$\eta = \frac{(\hat{\boldsymbol{z}} \times \mu_0 \boldsymbol{J}_h) \cdot (\nabla_h \phi + \nabla_h \psi \times \hat{\boldsymbol{z}} + B_z \boldsymbol{u}_h - v_z \boldsymbol{B}_h)}{|\mu_0 \boldsymbol{J}_h|^2}. \tag{17}$$

In the case of a resistive plasma, we obtain the same solutions as in the case of an ideal plasma, with the additional term η on the right-hand side. These equations stand for any magnetic field $\boldsymbol{B}$; no restriction has been made on $\boldsymbol{B}$. However, if the magnetic field $\boldsymbol{B}$ is a force-free field, it is parallel to the current density $\boldsymbol{J}$ so that $(\hat{\boldsymbol{z}} \times \mu_0 \boldsymbol{J}_h) \cdot \boldsymbol{B}_h = 0$. In this case, the above Euler–Lagrange equations (Equations (15) and (17)) have a vanishing term and can be written as

$$v_z = \frac{B_z^2\, u_z + \boldsymbol{B}_h \cdot (\nabla_h \phi + \nabla_h \psi \times \hat{\boldsymbol{z}} + B_z \boldsymbol{u}_h)}{|\boldsymbol{B}|^2}, \tag{18}$$

$$\nabla_h \cdot \left(\frac{\nabla_h \psi}{B_z^2} \right) = \nabla_h \cdot \left[\frac{\hat{z} \times (v_z \boldsymbol{B}_h - \nabla_h \phi - B_z \boldsymbol{u}_h + \eta(\hat{z} \times \mu_0 \boldsymbol{J}_h))}{B_z^2} \right], \tag{19}$$

$$\eta = \frac{(\hat{z} \times \mu_0 \boldsymbol{J}_h) \cdot (\nabla_h \phi + \nabla_h \psi \times \hat{z} + B_z \boldsymbol{u}_h)}{|\mu_0 \boldsymbol{J}_h|^2}, \tag{20}$$

where for numerical reasons, a lower limit of $|\mu_0 \boldsymbol{J}_h|$ must be imposed here. In 64-bit computing, we set it to $10^{-12}\ \mathrm{N\,A^{-1}\,m^{-2}}$.

To see the physical meaning of Equation (17) or (20), we can use Ohm's Law,

$$\boldsymbol{E} = -(\boldsymbol{v} \times \boldsymbol{B}) + \eta \mu_0 \boldsymbol{J}, \tag{21}$$

in which we can separate horizontal and vertical components using the Helmholtz decomposition (*e.g.* Equation (5)),

$$\begin{aligned} \boldsymbol{E}_h &= -\hat{z} \times \left[(v_z \boldsymbol{B}_h - B_z \boldsymbol{v}_h) \right] + \eta \mu_0 \boldsymbol{J}_h \\ &= \nabla_h \phi \times \hat{z} - \nabla_h \psi, \end{aligned} \tag{22}$$

$$E_z = \boldsymbol{v}_h \cdot (\hat{z} \times \boldsymbol{B}_h) + \eta \mu_0 J_z. \tag{23}$$

Equation (14) together with vector identity $\boldsymbol{A} \cdot (\boldsymbol{B} \times \boldsymbol{C}) = \boldsymbol{B} \cdot (\boldsymbol{C} \times \boldsymbol{A}) = \boldsymbol{C} \cdot (\boldsymbol{A} \times \boldsymbol{B})$ are combined with Equation (17). We then use Equation (22) to obtain

$$\eta = \frac{\mu_0 \boldsymbol{J}_h \cdot \boldsymbol{E}_h}{|\mu_0 \boldsymbol{J}_h|^2} + \frac{(B_z \boldsymbol{u}_h - v_z \boldsymbol{B}_h) \cdot (\hat{z} \times \mu_0 \boldsymbol{J}_h)}{|\mu_0 \boldsymbol{J}_h|^2}. \tag{24}$$

Multiplying Equation (23) for the vertical component E_z by $\mu_0 J_z$ and summing with Equation (24) gives

$$\begin{aligned} \eta &= \frac{\mu_0 \boldsymbol{J} \cdot \boldsymbol{E}}{|\mu_0 \boldsymbol{J}|^2} + \frac{\mu_0 \boldsymbol{J} \cdot (\boldsymbol{v} \times \boldsymbol{B})}{|\mu_0 \boldsymbol{J}|^2} \\ &= \frac{\mu_0 \boldsymbol{J} \cdot \boldsymbol{E}}{|\mu_0 \boldsymbol{J}|^2} - \frac{\boldsymbol{v} \cdot (\mu_0 \boldsymbol{J} \times \boldsymbol{B})}{|\mu_0 \boldsymbol{J}|^2}. \end{aligned} \tag{25}$$

Equation (25) could have been found using the scalar product of the generalized Ohm's law (Equation (21)) with $\mu_0 \boldsymbol{J}$.

In the context of the eddy diffusivity model, the difference between the two terms in Equation (25) represents the transport of magnetic flux from processes other than the resolved $\boldsymbol{v} \times \boldsymbol{B}$ electric field. The above derivation is relevant to any magnetic field $\boldsymbol{B}$. If, however, $\boldsymbol{B}$ is a force-free field, $\boldsymbol{J} \times \boldsymbol{B} = \boldsymbol{0}$ so that the last term of Equation (25) vanishes and we have

$$\eta = \frac{\mu_0 \boldsymbol{J} \cdot \boldsymbol{E}}{|\mu_0 \boldsymbol{J}|^2}. \tag{26}$$

The physical meaning of this equation is the same as in the case of a non-force-free magnetic field without considering the work done by the magnetic force. Rewriting Equation (25) leads to

$$\boldsymbol{J} \cdot \boldsymbol{E} = \frac{\eta |\mu_0 \boldsymbol{J}|^2}{\mu_0} - \boldsymbol{J} \cdot (\boldsymbol{v} \times \boldsymbol{B}). \tag{27}$$

Using the generalized Ohm's law (Equation (21)) and the magnetic flux conservation (Equation (1)), we obtain

$$\begin{aligned}\boldsymbol{J}\cdot\boldsymbol{E} &= \frac{\eta|\mu_0\boldsymbol{J}|^2}{\mu_0} - \boldsymbol{J}\cdot(\boldsymbol{v}\times\boldsymbol{B}) \\ &= -\frac{\boldsymbol{B}}{\mu_0}\cdot\frac{\partial\boldsymbol{B}}{\partial t} - \nabla\cdot\boldsymbol{P} \\ &= -\frac{1}{2}\frac{\partial B^2}{\partial t} - \nabla\cdot\boldsymbol{P},\end{aligned} \tag{28}$$

where $\boldsymbol{P}\equiv\frac{1}{\mu_0}(\boldsymbol{E}\times\boldsymbol{B})$ is the Poynting vector and Equation (28) is the differential form of the Poynting theorem (*e.g.* Griffiths, 2007). As a consequence, we can express η as a function of the Poynting vector,

$$\begin{aligned}\eta &= \frac{\mu_0\boldsymbol{J}\cdot\boldsymbol{E}}{|\mu_0\boldsymbol{J}|^2} + \frac{\mu_0\boldsymbol{J}\cdot(\boldsymbol{v}\times\boldsymbol{B})}{|\mu_0\boldsymbol{J}|^2} \\ &= \frac{\mu_0}{|\mu_0\boldsymbol{J}|^2}\left[-\frac{1}{2}\frac{\partial(\frac{|\boldsymbol{B}|^2}{\mu_0})}{\partial t} - \nabla\cdot\boldsymbol{P}\right] + \frac{\mu_0\boldsymbol{J}\cdot(\boldsymbol{v}\times\boldsymbol{B})}{|\mu_0\boldsymbol{J}|^2}.\end{aligned} \tag{29}$$

In the case of a force-free magnetic field, one obtains

$$\begin{aligned}\eta &= \frac{\mu_0\boldsymbol{J}\cdot\boldsymbol{E}}{|\mu_0\boldsymbol{J}|^2} \\ &= \frac{\mu_0}{|\mu_0\boldsymbol{J}|^2}\left[-\frac{1}{2}\frac{\partial(\frac{|\boldsymbol{B}|^2}{\mu_0})}{\partial t} - \nabla\cdot\boldsymbol{P}\right].\end{aligned} \tag{30}$$

4.4. Boundary Conditions for Magnetic Diffusivity $\eta(x, y)$

MEF takes boundary conditions in the form of a mask canceling values of $\phi(x, y)$ and $v_z(x, y)$ at pixels on the border of the domain that includes the active region, ∂AR. In MEF-R, we use a Hann window over eight grid points on the sides of the computational domain for all quantities except for the magnetic diffusivity $\eta(x, y)$. This produces an efficient mask, takes the whole area into consideration, and is compatible with the computation of vector magnetograms (Nakagawa and Raadu, 1972). Equations (18) and (20) are minimization forms of W according to v_z and η. Solving Equation (20) for η is done in the same way as solving Equation (18) for v_z.

4.5. Testing MEF-R: The Spheromak

Spheromaks are plasmas with internal magnetic fields but strong internal electric currents. They resemble a bipolar active region with twisted flux (Longcope, 2004). Due to finite magnetic diffusivity, they relax (Taylor, 1974) toward a state of minimal magnetic energy while conserving global magnetic helicity (Bellan, 2000). The consequence is that the magnetic field in the relaxed state is force-free (Bellan, 2000). Since the Spheromak is a closed system, the relaxed magnetic field is a linear force-free field (Woltjer, 1958). The relaxation process itself redistributes the current locally by reconnection processes (Garcia-Martinez, 2012) and is equivalent to the effect of eddy magnetic diffusivity. The latter would vanish when the system has reached the relaxed state but there would be still remaining uniform resistivity.

To create an analytical test for MEF-R we proceeded as follows. We use the magnetic vector field $(B_x, B_y, B_z)(x, y, z; t + \mathrm{d}t/2)$ from the Spheromak (Bellan, 2000) and an external velocity field $(v_x, v_y, v_z)(x, y, z; t + \mathrm{d}t/2)$ oriented in a single direction of space. We solved numerically the resistive magnetic induction equation (Equation (1)),

$$\frac{\partial \boldsymbol{B}}{\partial t} = \nabla \times \big[(\boldsymbol{v} \times \boldsymbol{B}) - \eta(\nabla \times \boldsymbol{B})\big],$$

using a second-order finite differences numerical discretization in space and a second-order leapfrog time-marching. This gives $(B_x, B_y, B_z)(x, y, z; t, t + \mathrm{d}t)$. Next, we used MEF-R with $(B_x, B_y, B_z)(x, y, z; t, t + \mathrm{d}t)$ and $v_r = v_z(x, y, z; t + \mathrm{d}t/2)$ to compute $(v_x, v_y, v_z)(x, y, z; t + \mathrm{d}t/2)$ and $\eta(x, y; t + \mathrm{d}t/2)$. We can then compare $(v_x, v_y, v_z)(x, y, z; t + \mathrm{d}t/2)$ (Figure 3(b)) and $\eta(x, y; t + \mathrm{d}t/2)$ (Figure 3(c)) with the original models.

As the test case Spheromak is purely analytical, we work in pixels (px) and dt units. The Spheromak has a radius $a = 20$ px and its center is located at $\boldsymbol{r}_\mathrm{c}(t) = (x_\mathrm{c}(t), y_\mathrm{c}(t), z_\mathrm{c}(t)) = (0, 0, -3)$ px. The generating flow is given as $\boldsymbol{v}(t + \mathrm{d}t/2) = 4\cos(35^\circ)\boldsymbol{e}_x + 4\sin(35^\circ)\boldsymbol{e}_y + 4\boldsymbol{e}_z$ with $|\boldsymbol{v}(t + \mathrm{d}t/2)| \approx 5.6\ \mathrm{px}\,\mathrm{d}t^{-1}$ (Figure 3(a)) and corresponds to a uniform translation of the Spheromak center along a constant direction (Longcope, 2004). A uniform magnetic diffusivity has been set to $\eta(x, y; t + \mathrm{d}t/2) = 10\ \mathrm{px}^2\,\mathrm{d}t^{-1}$. In Figure 3(a), we see only $v_{\perp x}$, $v_{\perp y}$, and $v_{\perp z}$ extracted from

$$v_\perp = \boldsymbol{v} - \big[(\boldsymbol{v} \cdot \boldsymbol{B})/\boldsymbol{B}^2\big]\boldsymbol{B},$$

the component of $\boldsymbol{v}$ perpendicular to the magnetic field lines. The vertical velocity field of the Spheromak $v_z(t + \mathrm{d}t/2)$ (Figure 3(a)) is similar to the MEF-R inferred flow $v_z(t + \mathrm{d}t/2)$ (Figure 3(b)). The inferred horizontal components of $\boldsymbol{v}$ are somehow different, however (see vectors in Figures 3(a) and 3(b)). This is a consequence of the decay of kinetic energy W during the MEF-R iterative process. If we define the kinetic energy of the Spheromak numerically as

$$W = \Sigma_{x,y}\big[v_x^2 + v_y^2 + (v_z - u_z)^2\big]$$

and take the reference velocity $\boldsymbol{u}_h = \boldsymbol{0}$ and $u_z = v_{\perp z}$, we find the kinetic energy of the generating flow $W_0(t + \mathrm{d}t/2) \approx 23540\ \mathrm{px}^2\,\mathrm{d}t^{-2}$ to be greater than the kinetic energy of the perpendicular component of the generating flow $W_\perp(t + \mathrm{d}t/2) \approx 15045\ \mathrm{px}^2\,\mathrm{d}t^{-2}$ as expected, the latter being itself greater than the kinetic energy of the inferred final state $W_\mathrm{f}(t + \mathrm{d}t/2) \approx 976\ \mathrm{px}^2\,\mathrm{d}t^{-2}$,

$$W_\mathrm{f} < W_\perp < W_0\cdot$$

Our translation of the Spheromak is not a state of minimal kinetic energy and MEF-R, searching a flow of minimal kinetic energy, is not supposed to produce an inferred velocity matching exactly the initial flow.

Equation (14) predicts that in the absence of a horizontal reference flow $\boldsymbol{u}_h = \boldsymbol{0}$, the inferred horizontal velocity $\boldsymbol{v}_h$ should be perpendicular to $(\hat{z} \times \mu_0 \boldsymbol{J}_h)$. In other words, under the LFF assumption, MEF-R predicts that the minimal kinetic energy configuration of $\boldsymbol{v}$ will be such that $\boldsymbol{v}_h$ and $\boldsymbol{B}_h$ are parallel. However, neither the generating flow, the perpendicular component of the generating flow, nor the reference flow would have their horizontal component being parallel to $\boldsymbol{B}_h$.

How MEF-R predicts the magnetic eddy diffusivity at time $(t + \mathrm{d}t/2)$ is shown in Figure 3(c). The mean value of the inferred magnetic diffusivity is almost unchanged with

$\langle\eta\rangle \approx 9\ \mathrm{px}^2\,\mathrm{d}t^{-1}$ although it is not uniform with a standard deviation of $12\ \mathrm{px}^2\,\mathrm{d}t^{-1}$. In Figure 3(c) we superimposed the field lines of $(\hat{z} \times \mu_0 \boldsymbol{J}_h)$ above the map of $\eta(x, y; t + \mathrm{d}t/2)$. We see that MEF-R distorts the magnetic diffusivity along these lines as can be seen from Equation (17).

4.6. Statistics of the Results

Finally, to have a global measure of the performance of MEF-R in the Spheromak test case, we computed the correlation coefficients between $v^{\mathrm{s}}_{\perp x,y,z}$ of the Spheromak and $v_{\perp x,y,z}$ inferred from MEF-R. We found

$$C\bigl(v^{\mathrm{s}}_{\perp x}, v_{\perp x}\bigr) \approx 0.285, \qquad C\bigl(v^{\mathrm{s}}_{\perp y}, v_{\perp y}\bigr) \approx 0.137, \qquad C\bigl(v^{\mathrm{s}}_{\perp z}, v_{\perp z}\bigr) \approx 0.571.$$

The mean $\langle\rangle$ and standard deviation $\sigma[\ \ ]$ of the difference between the Spheromak and inferred velocities are also computed. We found

$$\begin{aligned} &\bigl\langle v^{\mathrm{s}}_{\perp x} - v_{\perp x}\bigr\rangle \approx 2.108\ \mathrm{px}\,\mathrm{d}t^{-1}, \qquad \bigl\langle v^{\mathrm{s}}_{\perp y} - v_{\perp y}\bigr\rangle \approx 1.906\ \mathrm{px}\,\mathrm{d}t^{-1}, \\ &\bigl\langle v^{\mathrm{s}}_{\perp z} - v_{\perp z}\bigr\rangle \approx 1.529\ \mathrm{px}\,\mathrm{d}t^{-1}, \end{aligned}$$

and

$$\begin{aligned} &\sigma\bigl[v^{\mathrm{s}}_{\perp x} - v_{\perp x}\bigr] \approx 1.541\ \mathrm{px}\,\mathrm{d}t^{-1}, \qquad \sigma\bigl[v^{\mathrm{s}}_{\perp y} - v_{\perp y}\bigr] \approx 1.412\ \mathrm{px}\,\mathrm{d}t^{-1}, \\ &\sigma\bigl[v^{\mathrm{s}}_{\perp z} - v_{\perp z}\bigr] \approx 1.735\ \mathrm{px}\,\mathrm{d}t^{-1}. \end{aligned}$$

The correlation and accuracy are higher for the vertical component of velocity as expected with MEF-R although the standard deviation is also slightly higher. A global measurement of the velocity differences in terms of vectors would give a lower value but with the same standard deviation,

$$\bigl\langle\bigl|\mathbf{v}^{\mathrm{s}}_{\perp}\bigr| - |\mathbf{v}_{\perp}|\bigr\rangle \approx 3.471\ \mathrm{px}\,\mathrm{d}t^{-1}, \qquad \sigma\bigl[\bigl|\mathbf{v}^{\mathrm{s}}_{\perp}\bigr| - |\mathbf{v}_{\perp}|\bigr] \approx 1.762\ \mathrm{px}\,\mathrm{d}t^{-1}.$$

The distribution of the relative orientations between the two vector fields is given by $\langle\mathbf{v}^{\mathrm{s}}_{\perp} \cdot \mathbf{v}_{\perp}\rangle \approx 3.392\ \mathrm{px}^2\,\mathrm{d}t^{-2}$ with standard deviation $\sigma[\mathbf{v}^{\mathrm{s}}_{\perp} \cdot \mathbf{v}_{\perp}] \approx 6.201\ \mathrm{px}^2\,\mathrm{d}t^{-2}$. A better estimate is given by the average dot product of the normalized perpendicular velocities $\langle\frac{\mathbf{v}^{\mathrm{s}}_{\perp} \cdot \mathbf{v}_{\perp}}{|\mathbf{v}^{\mathrm{s}}_{\perp}||\mathbf{v}_{\perp}|}\rangle \approx 0.959$ which follows the Cauchy–Schwarz inequality (Schrijver *et al.*, 2006) and indicates that the two fields are mostly parallel. The results are not as good for the resistivity. The correlation coefficient, mean, and standard deviation of the difference between true and inferred values of the resistivity η are

$$C\bigl(\eta^{\mathrm{s}}, \eta\bigr) \approx 0.243, \qquad \bigl\langle\bigl|\eta^{\mathrm{s}}\bigr| - |\eta|\bigr\rangle \approx 6.134\ \mathrm{px}^2\,\mathrm{d}t^{-1}, \qquad \sigma\bigl[\bigl|\eta^{\mathrm{s}}\bigr| - |\eta|\bigr] \approx 7.752\ \mathrm{px}^2\,\mathrm{d}t^{-1},$$

with extremal values of the resistivity about 10 times greater (Figure 3(c)).

These results only reflect the fact that the external velocity and magnetic diffusivity we imposed for the relaxed Spheromak are rather arbitrary and not consistent with a state of minimal kinetic energy as previously defined. More statistics are computed (*e.g.* Schrijver *et al.*, 2006) and a comparison with the case when we not only impose u_z but also u_x and u_y are given in Tables 2 and 3 (Appendix A).

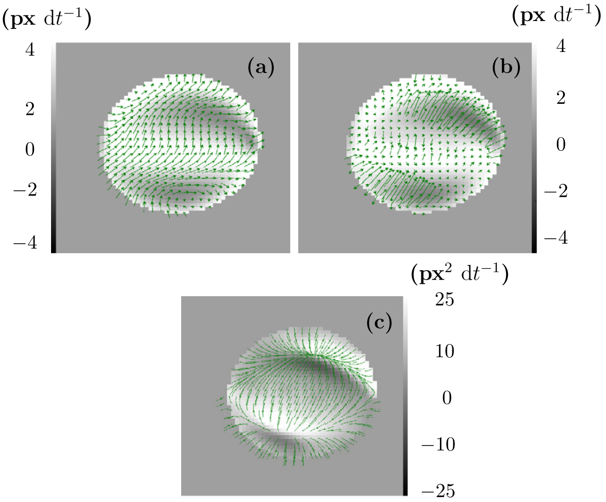

Figure 3 Testing MEF-R using the Spheromak at given time $t + \mathrm{d}t/2$ with a generating flow as a uniform velocity field $\boldsymbol{v}(t + \mathrm{d}t/2) = 4\cos(35^\circ)\boldsymbol{e}_x + 4\sin(35^\circ)\boldsymbol{e}_y + 4\boldsymbol{e}_z$. Here we show a cut in the plane $z = -3$ px. 2D vectors show the x- and y-components and the gray scale refers to the z-component. The Spheromak being closed, a circle is set to delimit the boundary. (a) The perpendicular components of the generating flow, $(v_{\perp x}, v_{\perp y})(x, y)$ (vectors) and $v_{\perp z}(x, y)$ (gray scale). (b) How MEF-R reconstructs the velocity field $(v_x, v_y)(x, y)$ (vectors) and $v_z(x, y)$ (gray scale). (c) Magnetic diffusivity $\eta_{\mathrm{eddy}}(x, y)$ as reconstructed by MEF-R (gray scale). Field lines of $(\hat{z} \times \mu_0 \boldsymbol{J}_h)$ are superimposed. MEF-R distorts η_{eddy} along these lines (see Equation (17)).

5. Data Processing Using MEF-R: AR 9077

In MEF, v_r can be used as a vertical background velocity. In MEF-R, we precisely adjust the magnetic diffusivity so that v_z is as close as possible to v_r. We want to compute both $\boldsymbol{v}(x, y)$ and $\eta(x, y)$. Whenever we had to compute $\frac{1}{B_z}$, the vertical component $B_z(x, y)$ was further thresholded, $|B_z(x, y)| \geqslant 40$ G, to avoid dividing by zero or computer round-off values. This value is chosen to be above the noise (≈ 20 G in our data).

5.1. Testing MEF-R: Numerical Convergence

Numerical simulations of reconnection processes in the lower corona have been done with a variable magnetic diffusivity $\eta(J)$ as an explicit function of current density J (*e.g.* Chen and Shibata, 2000; Otto, 2001) or $\eta(v_{\mathrm{ed}})$ varying with electron velocity v_{ed} (Miyagoshi and Yokoyama, 2004). However, to our knowledge no code simulating convection up to the photosphere and using the variable $\eta(x, y)$ is currently available. This is left for future work. Nevertheless, we did check numerically that the solution was indeed a unique solution to the magnetic induction equation. In Figure 4(a) we display the scaled residuals of the vertical component of the magnetic induction equation (Equation (3)). Here we have rescaled the residuals by the standard deviation of the variable $\frac{\partial B_z}{\partial t}$. Scales range from -10.7 to 11.2 with a mean value at 0.00239 and standard deviation of 0.9296. The convergence process itself is shown in Figure 4(b). The kinetic energy scale here is in $(\mathrm{px}\,\mathrm{d}t^{-1})^2$ (see Table 4 in Appendix B). The convergence is nearly obtained at 400 iterations. After 1000 iterations there is no significant improvement in the convergence.

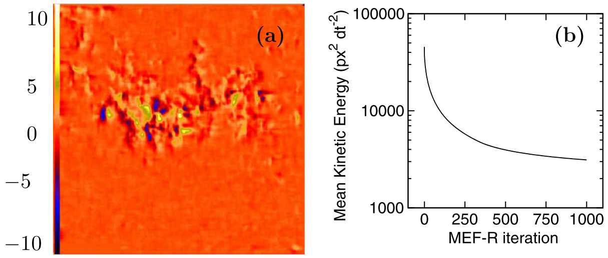

Figure 4 (a) Map of the scaled residuals of the vertical component of equation of conservation of magnetic flux (Equation (3)) corresponding to the time interval 08:00 – 09:36 UT of 14 July 2000 in AR 9077. Residuals have been rescaled by the standard deviation of the variable $\frac{\partial B_z}{\partial t}$. (b) Convergence curve of the MEF-R. Kinetic energy scale here is in $(\mathrm{px}\,\mathrm{d}t^{-1})^2$.

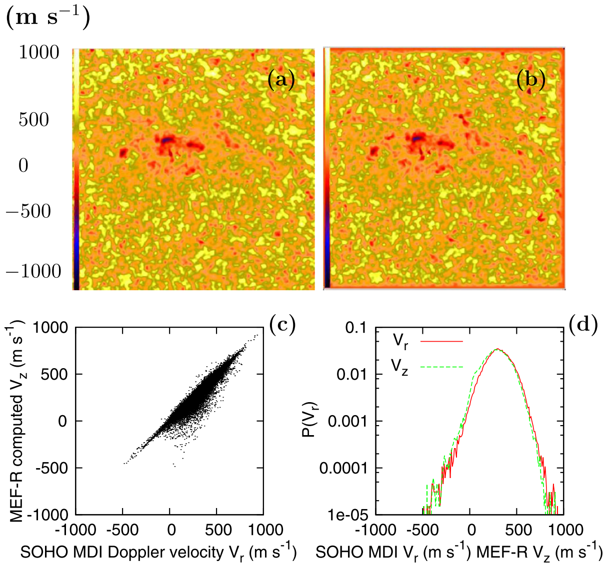

Figure 5 (a) Doppler velocity $v_r(t)$ in AR 9077 recorded by SOHO/MDI on 14 July 2000. The Sun's rotation has been removed. (b) $v_z(t)$ as computed using MEF-R with magnetic diffusivity $\eta(x, y; t)$ so that $v_z(t) \approx v_r(t)$. The time interval is 08:00 – 09:36 UT and the grid size is 256 × 256 pixels in both panels. Panel (c) shows the scatter plot between vertical velocity $v_z(t)$ computed using MEF-R and Doppler velocity $v_r(t)$. Panel (d) compares histograms of $v_z(t)$ and $v_r(t)$.

5.2. Vertical Velocity Versus Doppler Velocity

As expected, after 1000 iterations of MEF-R, we found that $v_z(t)$ is very close to Doppler velocity $v_r(t)$ (Figures 5(a) and 5(b)), in particular inside the active region. This is to be compared with Figure 2 where $v_z(x, y)$ was computed using MEF for a non-resistive ideal gas. There are still differences, however, as can be seen on a scatter plot (Figure 5(c)) due to iterative noise amplification by MEF-R of uncorrected bad pixels on the two vector magnetograms we used. This can be quantified using the histograms of $v_z(x, y; t)$ and $v_r(x, y; t)$ plotted in Figure 5(d) and occurs mostly for the highest values of velocity $|v_z(x, y; t)|$ although due to the minimization process v_z is slightly smaller than v_r. The correlation coefficients are $C(v_r, v_z) \approx 0.9937$ for $1\ \mathrm{G} \leqslant |B_\ell| \leqslant 2500\ \mathrm{G}$, with a weak field contribution $C(v_r, v_z) \approx 0.9939$ for $1\ \mathrm{G} \leqslant |B_\ell| \leqslant 200\ \mathrm{G}$, as good as its strong-field contribution $C(v_r, v_z) \approx 0.9909$ for $500\ \mathrm{G} \leqslant |B_\ell| \leqslant 2500\ \mathrm{G}$.

Figure 6 Velocity vector field (v_x, v_y) in AR 9077, 14 July 2000 between times 08:00 and 09:36 UT, computed with MEF-R after 1000 iterations using vector magnetograms and Doppler velocities from SOHO/MDI. Scales range over [0:200] $\mathrm{m\,s^{-1}}$. At strong-field locations spirals are rotating counterclockwise. The area is 500 × 500 $\mathrm{arcsec^2}$.

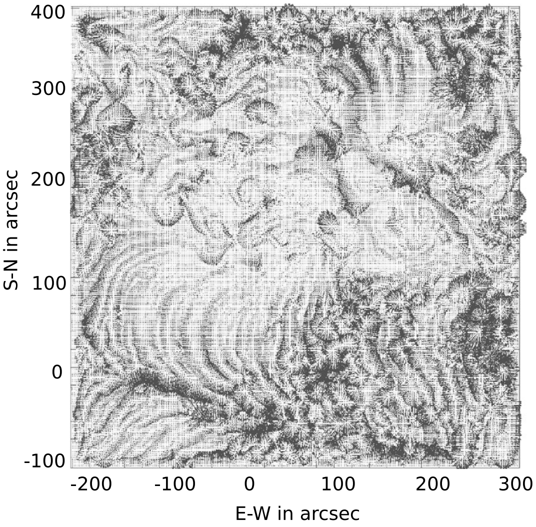

5.3. Horizontal Velocity

To compute $\boldsymbol{v}_h(x, y)$ we have used Equation (7). In Figure 6 we show the horizontal velocity vector field (v_x, v_y) computed with MEF-R using vector magnetograms and Doppler velocities between 08:00 and 09:36 UT. The use of a flat field constructed from $|\boldsymbol{v}_h(x, y)|$ as done for temperature T (Potts and Diver, 2009) would produce a cleaner and smoother picture. In the active region where (B_x, B_y, B_z) is strong the velocity is weaker, as expected given the stabilizing property of the magnetic field. Outside of the active region, the physics is more complex and, as noted by Longcope (2004), it is unlikely that we have computed the real velocity field.

An animation[1] depicting the evolution of the velocity fields shows that before the flare (*e.g.* 08:00 – 09:36 UT), there is extra vertical activity and little horizontal motions, with $|v_z|$ being much larger than $|\boldsymbol{v}_h|$. Quantitatively, the velocity vectors are mostly oriented vertically, with a maxima of $\approx 916\ \mathrm{m\,s^{-1}}$, a mean value of $\approx 286\ \mathrm{m\,s^{-1}}$ and a standard deviation of $\approx 121\ \mathrm{m\,s^{-1}}$. The maximal horizontal velocity is $\approx 199\ \mathrm{m\,s^{-1}}$, the mean is $\approx 18\ \mathrm{m\,s^{-1}}$, and the standard deviation is $\approx 23\ \mathrm{m\,s^{-1}}$.

It is the opposite at the time of the flare (10:30 – 11:12 UT). The motions are mostly horizontal and more chaotic, whereas vertical motions are more equally distributed and more coherent (not shown). During this lapse of time, the maximum value of the vertical velocity is $\approx 594\ \mathrm{m\,s^{-1}}$, the mean value is $\approx 121\ \mathrm{m\,s^{-1}}$, and the standard deviation is $\approx 81\ \mathrm{m\,s^{-1}}$. The maximum value of the horizontal velocity is $\approx 628\ \mathrm{m\,s^{-1}}$, the mean is $\approx 38\ \mathrm{m\,s^{-1}}$, and the standard deviation is $\approx 56\ \mathrm{m\,s^{-1}}$.

In this animation, at the time of the flare, chaotic flows occur everywhere in the active region and it is unclear whether it occurs mostly in the sunspots or around the polarity inversion lines. Note that the absorption line Ni I 6768 Å used to measure both Doppler and Zeeman shifts in SOHO/MDI could be perturbed by a strong flare and thus Doppler velocities and magnetic field values might not be accurate during a flare (*e.g.* Babin and Koval, 2007).

---

[1] Supplementary material available at: http://www.astro.umontreal.ca/~benoit/MEF-R.

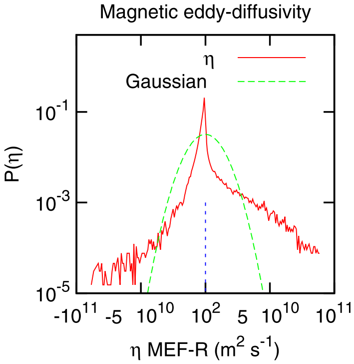

Figure 7 Histogram of the magnetic diffusivity $\eta(x, y)$ in AR 9077, 14 July 2000, 08:00 – 09:36 UT, compared with a Gaussian of the same variance. Exponential wings are the signature of intermittency. Log scale is used in the vertical axis. Mean value is $\approx 10^8\ \mathrm{m}^2\,\mathrm{s}^{-1}$ (vertical line). Standard deviation is $\sigma \approx 10^{10}\ \mathrm{m}^2\,\mathrm{s}^{-1}$. $|\eta(x, y)| \geqslant 2 \times 10^{10}\ \mathrm{m}^2\,\mathrm{s}^{-1}$ are due to noise.

5.4. Computation of the Magnetic Diffusivity

The values of eddy magnetic diffusivity $\eta(x, y)$ are sparse but can equally be positive or negative (see below) with a mean value of $\approx 10^8\ \mathrm{m}^2\,\mathrm{s}^{-1}$ and standard deviation of $\approx 10^{10}\ \mathrm{m}^2\,\mathrm{s}^{-1}$ (Figure 7). These values can be much larger than the largest values computed from magnetograms by Chae, Litvinenko, and Sakurai (2008) using a generalization of the nonlinear affine velocity estimator of Chae and Sakurai (2008) and a pixel size of about 2 arcsec (1400 km). Negative extrema of $\eta(x, y)$ may be partly due to noise in the data. Indeed, their amplitude could be reduced by using higher resolution data. In this case, they are unphysical. But some of the negative values of the diffusivity in Figure 8(a) are in strong magnetic field regions, where the relative error in field measurements is expected to be low. At these places, the action of negative eddy diffusivity would be to concentrate rather than disperse flux (*e.g.* Petrovay, 1994). Such an explanation has been given in the case of a theoretical dynamo (Zheligovsky, Podvigina, and Frisch, 2001).

Locally, high values of turbulent diffusivity are considered greater than $10^6\ \mathrm{m}^2\,\mathrm{s}^{-1}$ for the photosphere (*e.g.* Abramenko *et al.*, 2011) but values of $2.5 \times 10^8\ \mathrm{m}^2\,\mathrm{s}^{-1}$ have been inferred (Simon and Weiss, 1997) with a pixel of the size of a granule or larger. In fact, $\eta(x, y)$ could be even higher in the lower corona (Wu *et al.*, 2000) and the chromosphere (Miyagoshi and Yokoyama, 2004; Heggland, De Pontieu, and Hansteen, 2009).

The values of $\eta_{\min}$ and $\eta_{\max}$ are of the order of what we expect here for numerical-grid diffusivity $\mathrm{d}r^2\,\mathrm{d}t^{-1} \approx 3.9 \times 10^8\ \mathrm{m}^2\,\mathrm{s}^{-1}$, although below these values the value of the magnetic diffusivity is likely distorted.

The normalized histogram or probability distribution function of the magnetic diffusivity $\eta(x, y)$ between 08:00 and 09:36 UT is displayed on Figure 7 (solid line). It is different from a Gaussian distribution of the same variance (dashed line) but displays exponential wings characteristic of intermittency. The standard deviation is $\sigma \approx 10^{10}\ \mathrm{m}^2\,\mathrm{s}^{-1}$. At the start of a flare, the temperature distribution is observed to be chaotic (*e.g.* Veronig *et al.*, 2006). Since magnetic diffusivity depends on temperature (Spitzer, 1962), it is expected that the variance of the magnetic diffusivity will also increase. This is what we see at 10:30 UT, the time of the flare, and at 12:48 UT, at the beginning of the thermalization phase (see below in Section 6).

The map of the magnetic diffusivity is shown in Figure 8(a). Spiral structures can be seen at the location of sunspots where there are strong unipolar magnetic fields. These spirals rotate counterclockwise in AR 9077 (Figure 8(a)). The direction of rotation of these spirals is related to the sign of the average twist α. In an active region in the southern hemisphere where α would be positive, we predict that these spiral features would rotate clockwise. The physical mechanism of the observed hemispheric distribution of active region helicity has been proposed to be due to the action of the Coriolis force on a rising Ω-shaped flux tube originating deep inside the convection layer below an active region (Sakurai and Hagino, 2003).

For numerical reasons, $|\boldsymbol{J}_h| \geqslant 10^{-3}\ \mathrm{A\,m^{-2}}$ must be used in the computation. This lower threshold value roughly equals the noise level in our data. Moreover, to better focus on the active region itself and to reduce discretization effects involving terms in $1/B_z$ (Longcope, 2004) we have used a threshold value of $|J_z| \geqslant 10^{-2}\ \mathrm{A\,m^{-2}}$ in the computation of Equation (20). Such values of $|J_z|$ are observed at resolutions of 2.5 arcsec at the photosphere within sunspots (*e.g.* Krall *et al.*, 1982; Deloach *et al.*, 1984).

As can be seen in Equations (20) and (25), η_{eddy} is also a function of $\boldsymbol{J}$ and thus can be compared to $\eta(|\boldsymbol{J}|)$ (Otto, 2001). The peaks of $\eta(x, y)$ (Figure 8(a)) are located at the same places where photospheric currents are maximal (Figure 8(c)) and temperatures are minimal (Figure 11(b)) and where spiral centers are often located (Figures 6 and 8(a)). In fact, magnetic diffusivity in the photosphere and chromosphere can also be modeled as a function of temperature (Spitzer, 1962; Kumar, Kumar, and Uddin, 2011), $\eta(T) = c\,10^8 T^{-3/2}\ (\mathrm{m^2\,s^{-1}})$ where $c \approx 5$ is a constant (Figure 8(d)). Here we used the continuum intensity also measured by SOHO/MDI with the flat field corrected (Potts and Diver, 2009) to derive T (Solanki, Walther, and Livingston, 1993). We found that $\eta(T)$ and $\eta(|\boldsymbol{J}|)$ are correlated with $C(\eta(|\boldsymbol{J}|), \eta(T)) \approx 0.88$ for $100\ \mathrm{G} \leqslant |B_\ell| \leqslant 2000\ \mathrm{G}$ and especially for the strongest magnetic fields $1000\ \mathrm{G} \leqslant |B_\ell| \leqslant 2000\ \mathrm{G}$ with $C(\eta(|\boldsymbol{J}|), \eta(T)) \approx 0.98$. But η_{eddy} does not well correlate with neither $\eta(T)$ nor $\eta(|\boldsymbol{J}|)$. For $100\ \mathrm{G} \leqslant |B_\ell| \leqslant 2000\ \mathrm{G}$, we computed $C(\eta_{\mathrm{eddy}}, \eta(|\boldsymbol{J}|)) \approx 0.41$ and $C(\eta_{\mathrm{eddy}}, \eta(T)) \approx 0.56$. This is expected because the eddy diffusivity is not related to (molecular) resistivity but reflects the unresolved physics inside the subgrid.

To better understand the negative values of η_{eddy}, we have computed the corresponding map of angles between $\boldsymbol{J}$ and $\boldsymbol{E}$ (Figure 8(b)). A positive η occurs where angles are smaller than 90° whereas negative η is for angles greater than 90° and $\eta = 0$ corresponds to 90° between $\boldsymbol{J}$ and $\boldsymbol{E}$. Here η_{eddy}, $\boldsymbol{J}$, and $\boldsymbol{E}$ are eddy quantities representing macroscopic statistical effects, not actual processes.

5.5. The Meaning of η: Subgrid Eddy-Diffusivity

If magnetic diffusivity is small enough so that the velocity-dependent term is dominant in the generalized Ohm's law, we have

$$\begin{aligned} \boldsymbol{E} &= -(\boldsymbol{v} \times \boldsymbol{B}) + \eta_0 \mu_0 \boldsymbol{J} \\ &\approx -(\boldsymbol{v} \times \boldsymbol{B}), \end{aligned} \tag{31}$$

as in Longcope (2004). In such a case the MEF-R algorithm is able to compute v_z very close to v_r (Figure 5). But there are several places where the magnetic diffusivity takes negative values (Section 5.4). We have therefore to understand the physical meaning of $\eta_{\mathrm{eddy}}(x, y)$.

If the apparent diffusive effects of unresolved velocities are much greater than the advective transport of flux by velocities that can be resolved, then the electric field $\boldsymbol{E}$ can be modeled by resistivity only, namely

$$\begin{aligned} \boldsymbol{E} &= -(\boldsymbol{v} \times \boldsymbol{B}) + \eta_{\mathrm{eddy}} \mu_0 \boldsymbol{J} \\ &\approx \eta_{\mathrm{eddy}}\, \mu_0 \boldsymbol{J}. \end{aligned} \tag{32}$$

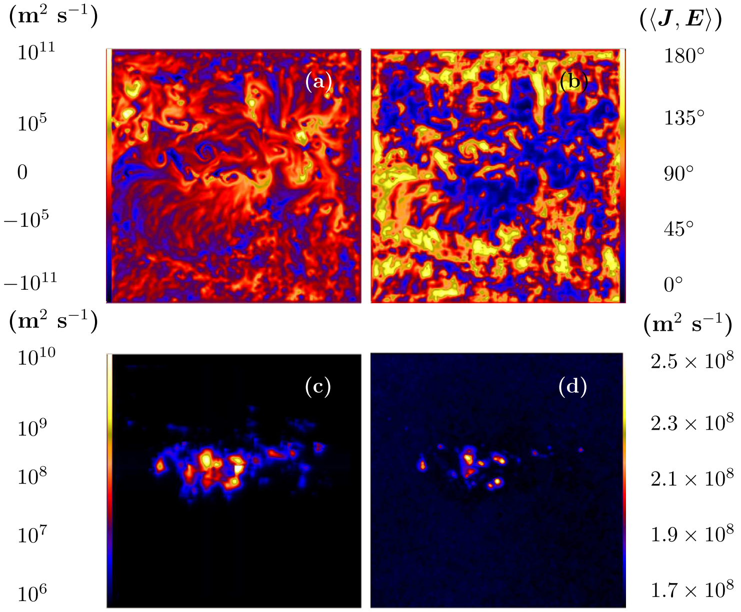

Figure 8 (a) Eddy diffusivity $\eta_{\mathrm{eddy}}(x, y)$ in AR 9077, 14 July 2000, computed with MEF-R using our modeled vector magnetic field and Doppler velocities at 08:00 and 09:36 UT. (b) Map of the angles between the vectors $\boldsymbol{J}$ and $\boldsymbol{E}$. (c) Magnetic diffusivity as a function of current density $J = |\boldsymbol{J}|$, $\eta(J) = k(J^2 - J_{\mathrm{c}}^2)^{1/2} S(J - J_{\mathrm{c}})\ \mathrm{m}^2\,\mathrm{s}^{-1}$ (Otto, 2001). (d) Magnetic diffusivity as a function of temperature T, $\eta(T) = c\,10^8 T^{-3/2}\ \mathrm{m}^2\,\mathrm{s}^{-1}$ (Spitzer, 1962).

Making the scalar product of both sides of Equation (32) with $\boldsymbol{J}$, we find an expression for η_{eddy},

$$\boldsymbol{J} \cdot \boldsymbol{E} \approx \mu_0 \eta_{\mathrm{eddy}} |\boldsymbol{J}|^2. \tag{33}$$

However, since we consider only force-free magnetic fields, $\boldsymbol{J}$ and $\boldsymbol{B}$ are parallel and we have a strict equality instead of an approximation. We can now write η_{eddy} as

$$\eta_{\mathrm{eddy}} = \frac{\boldsymbol{J} \cdot \boldsymbol{E}}{\mu_0 |\boldsymbol{J}|^2}. \tag{34}$$

Equation (34) is equivalent to Equation (26) that we derived from Euler–Lagrange formalism for η within the force-free approximation and η is thus a magnetic turbulent diffusivity $\eta \equiv \eta_{\mathrm{eddy}}$. The sign of η_{eddy} depends locally on the angle between the vectors $\boldsymbol{J}$ and $\boldsymbol{E}$. If the magnetic field is not force-free, the solution is given by Equations (15), (16), and (17) whereas if the magnetic field is a force-free field it is given by Equations (18), (19), and (20). The relative orientation between $\boldsymbol{J}$ and $\boldsymbol{E}$ would be different in the two cases but the physical meaning of $\boldsymbol{J} \cdot \boldsymbol{E} \leqslant 0$ has to be understood as a statistical macroscopic effect.

To reconstruct an exact velocity field, one would need to involve the conservation of total energy and momentum (Fisher *et al.*, 2010), *i.e.* to solve the full set of 3D MHD equations. However, in MEF-R we only use the vertical component of the magnetic induction equation. Using Equations (7) and (15) it can be shown that $(\boldsymbol{v} - \boldsymbol{u}) \cdot \boldsymbol{B} = 0$, a result which the original MEF algorithm also yields. Splitting the velocity $\boldsymbol{v}$ into two components, one parallel to the magnetic field ($\boldsymbol{v}_{\parallel}$) and one perpendicular to the magnetic field ($\boldsymbol{v}_{\perp}$), it can be shown that

$$\begin{aligned} 0 &= (\boldsymbol{v} - \boldsymbol{u}) \cdot \boldsymbol{B} \\ &= \left[(\boldsymbol{v}_\perp - \boldsymbol{u}_\perp) + (\boldsymbol{v}_\parallel - \boldsymbol{u}_\parallel)\right] \cdot \boldsymbol{B} \\ &= (\boldsymbol{v}_\parallel - \boldsymbol{u}_\parallel) \cdot \boldsymbol{B}, \end{aligned} \tag{35}$$

which implies that if the reference flow $\boldsymbol{u}$ has a component parallel to the magnetic field $\boldsymbol{B}$, then the inferred flow will be such that $\boldsymbol{v}_\parallel = \boldsymbol{u}_\parallel$. Therefore, unless the parallel component $\boldsymbol{v}_\parallel$ is provided through a reference flow, both MEF and MEF-R can only provide the component of the velocity which is perpendicular to the magnetic field ($\boldsymbol{v}_\perp$).

In this study, we have made the assumption that the observed Doppler velocity is entirely due to either ideal electric fields or to magnetic eddy diffusivity. Flux tubes are examples of loci where the plasma flows parallel to the magnetic field $|(\boldsymbol{v} \times \boldsymbol{B})| \approx 0$ and resistivity is negligible. This is only partially the case at the photospheric level. It is, however, mostly the case in sunspots where the field lines are almost vertical. There, parallel flows would most contribute to the Doppler shift. If the vector magnetic fields are correctly oriented, MEF should be able to reproduce $v_z \approx v_r$ but only by using externally specified flow field $(u_{\parallel x}, u_{\parallel y})$. It is when and where the flow cannot be perpendicular that MEF cannot adjust v_z to v_r. And this could be the case because we made a further assumption by using force-free magnetic fields. If the vector magnetic field is incorrectly oriented, a DDM technique might be unable to match v_z with v_r unless it utilizes some eddy diffusivity to do so. In this case, it would be spurious eddy diffusivity.

A simple subgrid model of turbulent diffusivity in the case of isotropic turbulence has been proposed by Smagorinsky (1963) and later generalized to magnetic diffusivity (Theobald, Fox, and Sofia, 1994). In this case, $\eta_{\mathrm{sg}} = C_{\mathrm{e}}\, \mathrm{d}r^2 |\boldsymbol{J}|$ is based on the hypothesis that the effect of subgrid current fluctuations is similar to eddy magnetic diffusivity (*e.g.* Lu, 1995; Otto, 2001; Klimas *et al.*, 2004) that can be activated only if $|\boldsymbol{J}| \geqslant J_{\mathrm{c}}$ (Figure 8(c)).

5.6. Spiral-like Structures and the Force-Free Assumption

The magnetic diffusivity η is characterized by the presence of various patterns including spiral-like structures (Figure 8(a)). As per Equation (14), with $\boldsymbol{u}_h = \boldsymbol{0}$, the minimization of the energy functional over the magnetic diffusivity $\eta(x, y)$ results in $\boldsymbol{v}_h$ and $(\hat{z} \times \mu_0 \boldsymbol{J}_h)$ being perpendicular, namely

$$(\hat{z} \times \mu_0 \boldsymbol{J}_h) \cdot \boldsymbol{v}_h = 0. \tag{36}$$

This implies that the resulting horizontal velocity $\boldsymbol{v}_h$ must be parallel to the horizontal current density $\boldsymbol{J}_h$, as both vector quantities are non-zero. Since the horizontal magnetic field $\boldsymbol{B}_h$ is parallel to $\boldsymbol{J}_h$ under the force-free approximation, we conclude that $\boldsymbol{v}_h$ and $\boldsymbol{B}_h$ must also be parallel.

Mathematically, the expression of the magnetic diffusivity η under the force-free approximation given by Equation (20) can locally be interpreted as the scalar component of the projection of the Helmholtz decomposition vector $(\nabla_h \phi + \nabla_h \psi \times \hat{z})$ on the rotated density current vector $(\hat{z} \times \mu_0 \boldsymbol{J}_h)$, normalized by $|\mu_0 \boldsymbol{J}_h|$,

$$\begin{aligned} \eta &= \frac{(\nabla_h \phi + \nabla_h \psi \times \hat{z}) \cdot (\hat{z} \times \mu_0 \boldsymbol{J}_h)}{|\mu_0 \boldsymbol{J}_h|^2} \\ &= \frac{1}{|\mu_0 \boldsymbol{J}_h|}\left[(\nabla_h \phi + \nabla_h \psi \times \hat{z}) \cdot \frac{(\hat{z} \times \mu_0 \boldsymbol{J}_h)}{|\mu_0 \boldsymbol{J}_h|}\right]. \end{aligned} \tag{37}$$

Here, $\frac{(\hat{z} \times \mu_0 \boldsymbol{J}_h)}{|\mu_0 \boldsymbol{J}_h|}$ is a unit vector.

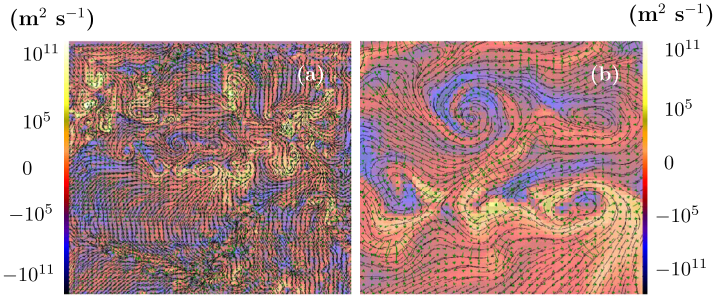

Figure 9 (a) Streamlines of rotated horizontal current density vector field ($\hat{z} \times \mu_0 \boldsymbol{J}_h$) together with vectors of inferred horizontal velocity $\boldsymbol{v}_h$ in AR9077, 14 July 2000, 08:00 – 09:36 UT, displayed over the map of magnetic eddy diffusivity $\eta(x, y)$. (b) An enlargement of the area near the center of the domain.

For a non-zero magnetic diffusivity, we expect the resulting map to be reminiscent of the structure of ($\hat{z} \times \mu_0 \boldsymbol{J}_h$) (Figure 9(a)). The vectors of $\boldsymbol{v}_h$, $\boldsymbol{B}_h$, and $\boldsymbol{J}_h$, as formulated within the LFF assumption, are found to be perpendicular to the streamlines of ($\hat{z} \times \mu_0 \boldsymbol{J}_h$) inside the photospheric plane. The streamlines of ($\hat{z} \times \mu_0 \boldsymbol{J}_h$) outline spiral-like structures on the map of the magnetic diffusivity (Figure 9(b)). This suggests that, as a result of Equation (37), spiral-like features seen in the maps of ($\hat{z} \times \mu_0 \boldsymbol{J}_h$) and consequently of $\eta(x, y)$ might be artifacts of the LFF approximation used to reconstruct the magnetic field of AR 9077.

6. Time Evolution: Catching the Flare

The time evolution of active region AR 9077 can be well traced using the time series of various physical quantities we can compute using MEF-R (Figure 10). Here $\langle\ .\ \rangle$ denotes an average over the entire area. Shortly before the flare (10:30 UT) there is a break in the motion of the plasma followed by a sharp upward motion just before and during the flare (Figure 10(a)). Observations as well as numerical simulations suggest the existence of such precursors in flaring active regions (Falchi and Mauas, 2002; Alexander, 2006; Ilonidis, Zhao, and Kosovichev, 2011; Archontis and Hood, 2012). Using semi-empirical models, Falchi and Mauas (2002) have shown that such motions of the chromosphere are needed to reproduce the time evolution of Si I 3905 Å and Ca II K line profiles. $\boldsymbol{E}$ and $\boldsymbol{J}$ are oriented in the opposite directions only during the flare, *i.e.* during a large scale reconnection event (Figure 10(b)). Similar to the vertical velocity, the turbulent magnetic diffusivity η (Figure 10(b)) decays before the flare and strongly increases at the time of the flare. This is seen also in both models $\eta(J)$ (Otto, 2001) and $\eta(T)$ (Spitzer, 1962) (Figures 10(b) and 10(c)). Observations of active regions have shown that photospheric magnetic fields may change significantly during flares (Sudol and Harvey, 2005) and thus must respond to coronal field restructuring (Wang and Liu, 2010). The scale of those changes increases with the flare intensity. In X-class flares, abrupt field changes with amplitudes up to 450 G have been detected (Petrie and Sudol, 2010).

The Poynting vector becomes almost vertical and directed upward during and just after the flare as can be seen when comparing the time evolution of $\langle|\boldsymbol{P}|\rangle$ and P_z (Figure 10(d)). It has been seen in active regions that upward Poynting flux corresponds to flux emergence and not global plasma motion (Fan *et al.*, 2011). Observations of Poynting flux across the photosphere in emerging active regions found similar values $P_z \geqslant 10^4\ \mathrm{W\,m^{-2}}$ (*e.g.* Liu and Schuck, 2012). Data-driven numerical simulations of the emergence of a flux tube have

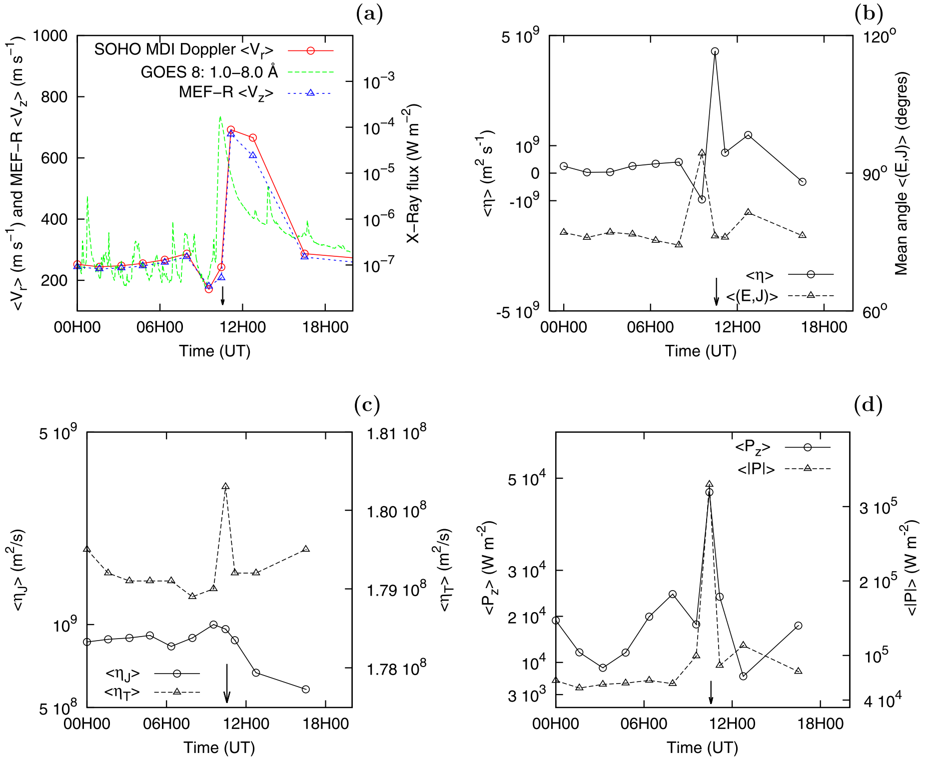

Figure 10 (a) Doppler velocity $\langle v_r \rangle$ observed with SOHO/MDI (red solid line with circles), the vertical velocity $\langle v_z \rangle$ computed with MEF-R (blue dashed line with triangles), and X-ray flux recorded by GOES 8 in the 1.0 – 8.0 Å channel (green dashed line) in AR 9077, on 14 July 2000. (b) Mean eddy magnetic diffusivity $\langle \eta \rangle$ computed by MEF-R (solid line with circles, scale on the left axis) and the mean angle $\langle \boldsymbol{E}, \boldsymbol{J} \rangle$ (dashed line with triangles, scale on the right axis). (c) Models of the magnetic diffusivity function; $\langle \eta(J) \rangle$ (solid line with circles) and $\langle \eta(T) \rangle$ (dashed line with triangles). (d) Poynting flux $\langle |\boldsymbol{P}| \rangle$ and its z-component $\langle P_z \rangle$. The arrows indicate the time of the flare (10:30 UT) in all the panels.

produced upward-directed vertical Poynting flux $\approx 10^6$ W m^{-2} with a steep increase during emergence to $\approx 10^7$ W m^{-2} on average over the area of the active region (Chen *et al.*, 2014). Here, the vertical component of the Poynting flux P_z is slightly oriented upwards on average except at the time of the flare where it is strongly upwards (Figure 10(d)). The peaks of $|\boldsymbol{P}|$, T, and $\eta(J)$ are found at the same places where B_z is also maximal (not shown). If the photospheric resistivity is due to electric currents this would mean that at least part of the photospheric temperatures are due to Joule heating. But this is not the case with our supergranular turbulent magnetic diffusivity. Most of the energy flux radiated at the photospheric level is located in areas close to sunspots as displayed in a map of the modulus of the Poynting vector $|\boldsymbol{P}|$ (Figure 11(a)). At these places, the temperature is lower (Figure 11(b)).

7. Conclusions

When using the force-free field approximation, the MEF technique does not produce vertical velocity fields close to the observed Doppler velocities even given a reference background

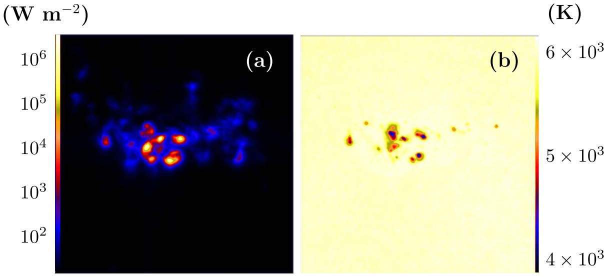

Figure 11 (a) Modulus of the Poynting flux $|\boldsymbol{P}|$ at the photospheric level in AR 9077, 14 July 2000, 08:00 – 09:36 UT. (b) Temperature map from continuum intensity recorded by SOHO/MDI. Scales range over [4000:6000] (K).

vertical velocity field. To address this point, we have supposed that, at least for a large scale (> 1.5 Mm), the photospheric magnetic field is not frozen-in to the plasma motions but that there must exist a magnetic eddy diffusivity term in the equation of magnetic flux conservation. We generalized the theory of MEF (Longcope, 2004) to include a resistive term in Ohm's Law.

Although our formulation is valid for any magnetic field $\boldsymbol{B}$, we had to limit our algorithm to the particular case of force-free magnetic fields. There are two reasons for that. The first reason is that, in the case of AR 9077, we had only access to SOHO/MDI line-of-sight magnetograms that we identify with the vertical component of the magnetic field. The second reason is that MEF-R needs the vertical derivatives of the magnetic field components and here too the force-free hypothesis was a way of solving the problem.

But the force-freeness of the photosphere is now questionable (Liu, Zhao, and Schuck, 2013) and DDM would overcompensate by creating a spurious eddy diffusivity. The reason is that parallel flows ($|(\boldsymbol{v} \times \boldsymbol{B})| \approx 0$) might contribute to the Doppler shift while being unrelated to either the diffusivity or the ideal electric field.

The algorithm could not be tested by comparison with other techniques because all of them, although they are able to process non-force-free vector magnetograms, are written for ideal MHD. Neither could we access local maps of observations of the magnetic diffusivity on the photosphere. But we used the analytical solution of the Spheromak (Bellan, 2000) and verified that MEF-R partly reconstructs the input fields in the induction equation.

We focused on the particular active region AR 9077 on 14 July 2000 and used line-of-sight magnetograms together with Doppler velocities as recorded by SOHO/MDI. Although we removed the differential rotation of the Sun and the limb effect, there is still a slight distortion effect due to sphericity. However, the effect would be small because on 14 July 2000, AR 9077 was close to the center of the solar disk. We indeed found that MEF-R gives a very good match between the computed v_z and the observed v_r. However, we found that our computed magnetic diffusivity $\eta(x, y)$ is in fact a turbulent diffusivity $\eta_{\mathrm{eddy}}(x, y)$ that could take negative values at some places. Nevertheless, on average over the whole area, most of the time we found positive and realistic values for η_{eddy}, in particular near the active region. The spatial distribution of $\eta_{\mathrm{eddy}}(x, y)$ is not well correlated with a model based on temperature $\eta(T)(x, y)$, but the correlation is still better than with a model based on a critical current density $\eta(|\boldsymbol{J}|)(x, y)$. The correlation coefficients here are less than 0.41 and are valid for strong magnetic fields ($100\ \mathrm{G} \leqslant |B_\ell| \leqslant 2000\ \mathrm{G}$). Nevertheless, an interesting result is that $\eta_{\mathrm{eddy}}(x, y)$ maps display spiral structures near the loci of strongest unipolar magnetic field. However, such structures might be the result of the linear force-free assumption that was used to reconstruct the vector magnetograms of AR 9077.

If anomalous Doppler broadening observed in spectral lines of the photosphere is due to microturbulent velocities, we could then predict a 2D spatial correlation with the high values of our inferred eddy diffusivity. Such a correlation would validate our model. For this purpose, we are currently using high resolution SOLIS/VSM spectral datacubes.

A generalization of the method to non-force-free magnetic fields is straightforward and under way but the problem of the first order vertical derivatives still needs to be solved. The divergence-free condition on the magnetic field together with the Zeeman effect measured in spectropolarimetric observations of two lines Fe I 6301.5 and 6302.5 Å formed at different depths (Bommier *et al.*, 2011) may be the key to this problem. In any case, at least to test the whole process, it is possible to use the 3D output of a radiative MHD simulation including a given model of the magnetic diffusivity (*e.g.* Abbett, 2007; Abbett and Fisher, 2012) for at least in the upper part of Sun's convection zone including the photosphere and data driven by magnetograms and Doppler velocities (Vincent, Charbonneau, and Dubé, 2012).

Acknowledgements Alain Vincent is supported through NSERC Individual Research Grant. Computations have been done with a modified version of MEF (Longcope, 2004). We have used the IDL graphics system and SAO Image DS9 from the Smithsonian Astrophysical Observatory. In this study, we have used SOHO/MDI data archives (http://soi.stanford.edu/data/) as well as Solar Monitor (http://www.solarmonitor.org/). We thank Frédérique Baron, Léonie Petitclerc, and Benoît Rolland for their initial contributions to data processing. Finally, we thank the anonymous reviewer for her/his constructive remarks.

Appendix A: Figures of Merit for the Spheromak Test

Statistical quantities are computed to test the accuracy of MEF-R in the Spheromak case. Only the perpendicular components of velocity are considered here. Given two 2D spatial scalar fields $F(x,y)$ and $f(x,y)$, we have computed the following quantities (*e.g.* Schrijver *et al.*, 2006): the coefficient of correlation,

$$C = \left[\Sigma_{x,y} F^{\mathrm{s}}(x,y)\cdot f(x,y)\right] \Big/ \left[\Sigma_{x,y} F^{\mathrm{s}}(x,y)^2 \Sigma_{x,y} f(x,y)^2\right]^{1/2},$$

the normalized error,

$$E_{\mathrm{N}} = \Sigma_{x,y}\left|f(x,y) - F^{\mathrm{s}}(x,y)\right| \Big/ \Sigma_{x,y}\left|F^{\mathrm{s}}(x,y)\right|,$$

and the mean error,

$$E_{\mathrm{M}} = \frac{1}{N}\Sigma_{x,y}\left[\left|f(x,y) - F^{s}(x,y)\right| \Big/ \left|F^{s}(x,y)\right|\right].$$

Here E_{M} and E_{N} are measures of differences between the two scalar fields. The ratio of "energies",

$$\epsilon = \Sigma_{x,y} f(x,y)^2 / \Sigma_{x,y} F^{s}(x,y)^2$$

is a measure of how well the model estimates the quadratic norm of the field. The "Cauchy–Schwarz inequality",

$$C_{\mathrm{CS}} = \frac{1}{N}\Sigma_{x,y}\left[F^{\mathrm{s}}(x,y)\cdot f(x,y)\right] \Big/ \left[\left|F^{\mathrm{s}}(x,y)\right|\left|f(x,y)\right|\right]$$

is a dimensionless measure of the relative orientation between the two vector fields. In the above formulas $F^{\mathrm{s}}(x,y)$ is an "exact" analytical Spheromak scalar field and $f(x,y)$ is the corresponding scalar field inferred from MEF. N is the number of grid points in (x,y).

Table 2 Various statistics to test the accuracy of MEF-R in the Spheromak case. The coefficient of correlation C, normalized error E_{N}, mean error E_{M}, ratio of "energies" ϵ, and Cauchy–Schwarz inequality (*e.g.* Schrijver *et al.*, 2006) are shown here for each component of the velocity and for the resistivity. Only the perpendicular component of velocity is considered here. For comparison purposes, the case where all three components (u_x, u_y, u_z) are taken as background velocities is shown in the right column.

$(v^{\mathrm{S}}_{\perp x}, v_{\perp x})$	u_z	u_x, u_y, u_z
C	0.2849	0.49079
E_{N}	0.9251	0.70102
E_{M}	1.6586	1.50043
ϵ	0.0175	0.27333
C_{CS}	0.3911	0.94217
$(v^{\mathrm{S}}_{\perp y}, v_{\perp y})$	u_z	u_x, u_y, u_z
C	0.1375	0.6107
E_{N}	0.8664	0.5842
E_{M}	1.3520	1.3586
ϵ	0.0426	0.3513
C_{CS}	0.2619	0.9251
$(v^{\mathrm{S}}_{\perp z}, v_{\perp z})$	u_z	u_x, u_y, u_z
C	0.5708	0.5741
E_{N}	0.6517	0.6582
E_{M}	1.9979	1.6309
ϵ	0.3464	0.3102
C_{CS}	0.9591	0.9761
$(\eta^{\mathrm{S}}, \eta)$	u_z	u_x, u_y, u_z
C	0.2434	0.4999
E_{N}	0.7928	0.6836
E_{M}	1.7928	1.6836
ϵ	0.7237	0.4002
C_{CS}	0.4047	0.9693

The coefficient of correlation C, normalized error E_{N}, mean error E_{M}, and ratio of "energies" ϵ are shown in Table 2 for each component of the velocity and for the resistivity. In Table 3 we display the mean and standard deviation of the difference between scalar or vector velocity fields corresponding to the "exact" Spheromak and MEF-R-based fields. In both Tables 2 and 3 we have compared two cases. First (left column), we impose u_z only as a background velocity. Second (right column), we impose all three components (u_x, u_y, u_z).

Appendix B: Conversion of Units

In MEF, time and space units are $\mathrm{d}t = t_2 - t_1$ and pixels (px). Conversion formulas to SI units are listed in Table 4. Here B is the magnetic induction, t is the time, v is the velocity, E is the electric field, P is the Poynting flux, μ_0 is the magnetic permeability, I and J are the current and the current density, ϕ and ψ are electric potentials, η is the magnetic diffusivity, n is the number of gridpoints in each direction of 2D space, $\mathrm{d}t$ is the time between two consecutive magnetograms, L is the size of the area under study, and px stands for the size of a 'pixel'.

Table 3 Various statistics to test the accuracy of MEF-R in the Spheromak case. Mean and standard deviation of (i) the angle distribution between "exact" Spheromak and MEF-R-based velocity vectors, (ii) the difference between scalar or vector fields corresponding to "exact" Spheromak and MEF-R-based fields, and (iii) the difference between magnetic diffusivities based on the "exact" Spheromak and MEF-R. Only the perpendicular components of velocity are considered here. For comparison purposes, the case where all three components (u_x, u_y, u_z) are taken as background velocities is shown in the right column.

	u_z	u_x, u_y, u_z
$\langle \mathbf{v}^{\mathrm{s}}_{\perp} \cdot \mathbf{v}_{\perp} \rangle$	3.39238	$6.86488\ \mathrm{px}^2\,\mathrm{d}t^{-2}$
$\sigma[\mathbf{v}^{\mathrm{s}}_{\perp} \cdot \mathbf{v}_{\perp}]$	6.20118	11.0127
$\langle \lvert\mathbf{v}^{\mathrm{s}}_{\perp}\rvert - \lvert\mathbf{v}_{\perp}\rvert \rangle$	3.47194	$2.99564\ \mathrm{px}\,\mathrm{d}t^{-1}$
$\sigma[\lvert\mathbf{v}^{\mathrm{s}}_{\perp}\rvert - \lvert\mathbf{v}_{\perp}\rvert]$	1.76250	2.26999
$\langle v^{\mathrm{s}}_{\perp x} - v_{\perp x} \rangle$	2.10845	1.52082
$\sigma[v^{\mathrm{s}}_{\perp x} - v_{\perp x}]$	1.54141	1.64542
$\langle v^{\mathrm{s}}_{\perp y} - v_{\perp y} \rangle$	1.90684	1.35509
$\sigma[v^{\mathrm{s}}_{\perp y} - v_{\perp y}]$	1.41212	1.43074
$\langle v^{\mathrm{s}}_{\perp z} - v_{\perp z} \rangle$	1.52915	1.56027
$\sigma[v^{\mathrm{s}}_{\perp z} - v_{\perp z}]$	1.73518	1.70398
$\langle \lvert\eta^{\mathrm{s}}\rvert - \lvert\eta\rvert \rangle$	6.13462	$6.83447\ \mathrm{px}^2\,\mathrm{d}t^{-1}$
$\sigma[\lvert\eta^{\mathrm{s}}\rvert - \lvert\eta\rvert]$	7.75257	5.73199

Table 4 Conversion factors from MKSA to MEF.

Quantity	MEF	MKSA	Conversion factor from MKSA to MEF
B	G	T	10^4
L	px	m	$(n\,L^{-1})$
t	$\mathrm{d}t$	s	$\mathrm{d}t$
v	$\mathrm{px}\,\mathrm{d}t^{-1}$	$\mathrm{m\,s^{-1}}$	$(n\,L^{-1})\,\mathrm{d}t$
E	$\mathrm{G\,px}\,\mathrm{d}t^{-1}$	$\mathrm{T\,m\,s^{-1}}$	$10^4\,\mathrm{d}t\,(n\,L^{-1})$
P	$\mathrm{kg}\,\mathrm{d}t^{-3}$	$\mathrm{kg\,s^{-3}}$	$\mathrm{d}t^3$
μ_0	$\mathrm{px\,G^2}\,\mathrm{d}t^2\,\mathrm{kg^{-1}}$	$\mathrm{m\,T^2\,s^2\,kg^{-1}}$	$10^8\,(n\,L^{-1})\,\mathrm{d}t^{-2}$
$\mu_0 J$	$\mathrm{G\,px^{-1}}$	$\mathrm{T\,m^{-1}}$	$10^4\,(L\,n^{-1})$
J	$\mathrm{kg\,G^{-1}}\,\mathrm{d}t^{-2}\,\mathrm{px^{-2}}$	$\mathrm{kg\,T^{-1}\,s^{-2}\,m^{-2}}$	$10^{-4}\,\mathrm{d}t^2\,(L^2\,n^{-2})$
ϕ, ψ	$\mathrm{G\,px^2}\,\mathrm{d}t^{-1}$	$\mathrm{T\,m^2\,s^{-1}}$	$10^4\,\mathrm{d}t\,(n^2\,L^{-2})$
η	$\mathrm{px^2}\,\mathrm{d}t^{-1}$	$\mathrm{m^2\,s^{-1}}$	$\mathrm{d}t\,(n^2\,L^{-2})$
I	$\mathrm{kg\,G^{-1}}\,\mathrm{d}t^{-2}$	$\mathrm{kg\,T^{-1}\,s^{-2}}$	$10^{-4}\,\mathrm{d}t^2$

References

Abbett, W.P.: 2007, The magnetic connection between the convection zone and corona in the quiet Sun. *Astrophys. J.* **665**, 1469.

Abbett, W.P., Fisher, G.H.: 2012, Radiative cooling in MHD models of the quiet Sun convection zone and corona. *Solar Phys.* **277**, 3.

Abramenko, V.I., Carbone, V., Yurchyshyn, V., Goode, P.R., Stein, R.F., Lepreti, F., Capparelli, V., Vecchio, A.: 2011, Turbulent diffusion in the photosphere as derived from photospheric bright point motion. *Astrophys. J.* **743**, 133.

Alexander, D.: 2006, An introduction to the pre-CME corona. *Space Sci. Rev.* **123**, 81.

Alfvén, H.: 1942, On the existence of electromagnetic-hydromagnetic waves. *Ark. Mat. Astron. Fys.* **29B**, 1.

Archontis, V., Hood, A.W.: 2012, Magnetic flux emergence: a precursor of solar plasma expulsion. *Astron. Astrophys.* **537**, A62.

Aschwanden, M.J.: 2008, Solar flare physics enlivened by TRACE and RHESSI. *Solar Phys.* **29**, 115.

Babin, A.N., Koval, A.N.: 2007, Ni I 6768 Å line profile variations during a solar flare and their effect on the SOHO/MDI magnetic field measurement. *Bull. Crimean Astrophys. Obs.* **103**, 63.

Bellan, P.M.: 2000, *Spheromaks. A Practical Application of Magnetohydrodynamic Dynamos and Plasma Self-Organization*, Imperial College Press, London, 71.

Bellot Rubio, L.R., Rodriguez Hidalgo, I., Collados, M., Khomenko, E., Ruiz Cobo, B.: 2001, Observation of convective collapse and upward-moving shocks in the quiet Sun. *Astrophys. J.* **560**, 1010.

Bommier, V., Degl'Innocenti, E.L., Schmieder, B., Gelly, B.: 2011, Vector magnetic field and vector current density in and around the δ-spot NOAA 10808. In: Choudhary, D.P., Strassmeier, K.G. (eds.) *The Physics of Sun and Star Spots*, *IAU Symp.* **273**, 338.

Brownstein, K.R.: 1994, Nonexistence of spatially bounded force-free magnetic fields: A scaling point of view. *IEEE Trans. Plasma Sci.* **22**, 275.

Büchner, J., Nikutowski, B., Otto, A.: 2004, Magnetic coupling of photosphere and corona: MHD simulation for multi-wavelength observations. In: Stepanov, A.V., Benevolenskaya, E.E., Kosovichev, A.G. (eds.) *Multi-Wavelength Investigations of Solar Activity*, *IAU Symp.* **223**, 353.

Cameron, R., Vögler, A., Schüssler, M.: 2011, Decay of a simulated mixed-polarity magnetic field in the solar surface layers. *Astron. Astrophys.* **533**, A86.

Cao, W., Goode, P.R., Ahn, K., Gorceix, N., Schmidt, W., Lin, H.: 2012, NIRIS – The second generation near-infrared imaging spectro-polarimeter for the 1.6 meter New Solar Telescope. In: Rimmele, T., Tritschler, A., Wöger, F., Collados, V., Socas-Navarro, H., Schlichenmaier, R., Carlsson, M., Berger, T., Cadavid, A., Gilbert, P., Goode, P., Knölker, M. (eds.) *2nd ATST-EAST Workshop in Solar Physics: Magnetic Fields from the Photosphere to the Corona*, *ASP Conf. Ser.* **463**, 291.

Chae, J., Litvinenko, Y.E., Sakurai, T.: 2008, Determination of magnetic diffusivity from high-resolution solar magnetograms. *Astrophys. J.* **683**, 1153.

Chae, J., Sakurai, T.: 2008, A test of three optical flow techniques-LCT, DAVE, and NAVE. *Astrophys. J.* **689**, 593.

Chen, P.F., Shibata, K.: 2000, An emerging flux trigger mechanism for coronal mass ejections. *Astrophys. J.* **545**, 524.

Chen, F., Peter, H., Bingert, S., Cheung, M.C.M.: 2014, A model for the formation of the active region corona driven by magnetic flux emergence. arXiv.

Chertok, I.M., Grechnev, V.V.: 2005, Large-scale activity in the Bastille day 2000 solar event. *Solar Phys.* **229**, 95.

Contopoulos, I., Kalapotharakos, C., Georgoulis, M.K.: 2011, Nonlinear force-free reconstruction of the global solar magnetic field: methodology. *Solar Phys.* **269**, 351.

Deloach, A.C., Hagyard, M.J., Rabin, D., Moore, R.L., Smith, B.J. Jr., West, E.A.: 1984, Photospheric electric current and transition region brightness within an active region. *Solar Phys.* **91**, 235.

DeRosa, M.L., Schrijver, C.J., Barnes, G., Leka, K.D., Lites, B.W., Aschwanden, M.J., Amari, T., Canou, A., McTiernan, J.M., Régnier, S., Thalmann, J.K., Valori, G., Wheatland, M.S., Wiegelmann, T., Cheung, M.C.M., Conlon, P.A., Fuhrmann, M., Inhester, B., Tadess, T.: 2009, A critical assessment of nonlinear force-free field modeling of the solar corona for active region 10953. *Astrophys. J.* **696**, 1780.

Falchi, A., Mauas, P.J.D.: 2002, Chromospheric models of a solar flare including velocity fields. *Astron. Astrophys.* **387**, 678.

Fan, Y., Zweibel, E.G., Linton, M.G., Fisher, G.H.: 1999, The rise of kink-unstable magnetic flux tubes and the origin of δ-configuration sunspots. *Astrophys. J.* **521**, 460.

Fan, Y.L., Wang, H.N., He, H., Zhu, X.S.: 2011, Study of the Poynting flux in active region 10930 using data-driven magnetohydrodynamic simulation. *Astrophys. J.* **737**, 39 (9 pp.).

Fisher, G.H., Welsch, B.T., Abbet, W.P.: 2012b, Can we determine electric fields and Poynting fluxes from vector magnetograms and Doppler measurements? *Solar Phys.* **277**, 153.

Fisher, G.H., Welsch, B.T., Abbett, W.P., Bercik, D.J.: 2010, Estimating electric fields from vector magnetogram sequences. *Astrophys. J.* **715**, 242.

Fisher, G.H., Bercik, D.J., Welsch, B.T., Hudson, H.S.: 2012a, Global forces in eruptive solar flares: the Lorentz force acting on the solar atmosphere and the solar interior. *Solar Phys.* **277**, 56.

Fuhrmann, M., Seehafer, N., Valori, G., Wiegelmann, T.: 2011, A comparison of preprocessing methods for solar force-free magnetic field extrapolation. *Astron. Astrophys.* **526**, A70.

Garcia-Martinez, P.L.: 2012, Dynamics of magnetic relaxation in Spheromaks. In: Zheng, L. (ed.) *Topics in Magnetohydrodynamics*, InTech, Rijeka, 85.

Georgoulis, M.K., LaBonte, B.J.: 2005, Reconstruction of an inductive velocity field vector from Doppler motions and a pair of solar vector magnetograms. *Astrophys. J.* **636**, 475.

Griffiths, D.J.: 2007 *Introduction to Electrodynamics*, Harlow, Essex, 345, 555.

Hao, J., Zhang, M.: 2011, Hemispheric helicity trend for solar cycle 24. *Astrophys. J. Lett.* **733**, L27.

Harra, L.K., Archontis, V., Pedram, E., Hood, A.W., Shelton, D.L., van Driel-Gesztelyi, L.: 2012, The creation of outflowing plasma in the corona at emerging flux regions: Comparing observations and simulations. *Solar Phys.* **278**, 47.

Hathaway, D.H., Beck, J.G., Bogart, R.S., Bachmann, K.T., Khatri, G., Petitto, J.M., Han, S., Raymond, J.: 2000, The photospheric convection spectrum. *Solar Phys.* **193**, 299.

Heggland, L., De Pontieu, B., Hansteen, V.H.: 2009, Observational signatures of simulated reconnection events in the solar chromosphere and transition region. *Astrophys. J.* **702**, 1.

Ilonidis, S., Zhao, J., Kosovichev, A.: 2011, Detection of emerging sunspot regions in the solar interior. *Science* **333**, 993.

Keller, C.U., Solis Team: 2001, The SOLIS Vector-Spectromagnetograph (VSM). In: Sigwarth, M. (ed.) *Advanced Solar Polarimetry – Theory, Observation, and Instrumentation*, *ASP Conf. Ser.* **236**, 16.

Klimas, A.J., Uritsky, V.M., Vassiliadis, D., Baker, D.N.: 2004, Reconnection and scale-free avalanching in a driven current-sheet model. *J. Geophys. Res.* **109**, 2218.

Kosugi, T., Matsuzaki, K., Sakao, T., Shimizu, T., Sone, Y., Tachikawa, S., Hashimoto, T., Minesugi, K., Ohnishi, A., Yamada, T., Tsuneta, S., Hara, H., Ichimoto, K., Suematsu, Y., Shimojo, M., Watanabe, T., Shimada, S., Davis, J.M., Hill, L.D., Owens, J.K., Title, A.M., Culhane, J.L., Harra, L.K., Doschek, G.A., Golub, L.: 2007, The Hinode (Solar-B) mission: An overview. *Solar Phys.* **243**, 3.

Krall, K.R., Smith, J.B. Jr., Hagyard, M.J., West, E.A., Cummings, N.P.: 1982, Vector magnetic field evolution, energy storage, and associated photospheric velocity shear within a flare-productive active region. *Solar Phys.* **79**, 59.

Kumar, P., Kumar, N., Uddin, W.: 2011, Reconnection in photospheric-chromospheric current sheet and coronal heating. *Plasma Phys. Rep.* **37**, 161.

Lantz, S.R., Fan, Y.: 1999, Anelastic magnetohydrodynamic equations for modeling solar and stellar convection zones. *Astron. Astrophys. Suppl.* **121**, 247.

Liu, Y., Schuck, P.W.: 2012, Magnetic energy and helicity in two emerging active regions in the Sun. *Astrophys. J.* **761**, 105.

Liu, Y., Zhang, H.: 2001, Relationship between magnetic field evolution and major flare event on July 14, 2000. *Astron. Astrophys.* **372**, 1019.

Liu, Y., Zhao, J., Schuck, P.W.: 2013, Horizontal flows in the photosphere and subphotosphere of two active regions. *Solar Phys.* **287**, 279.

Longcope, D.W.: 2004, Inferring a photospheric velocity field from a sequence of vector magnetograms: The minimum energy fit. *Astrophys. J.* **612**, 1181.

Lu, E.T.: 1995, Avalanches in continuum driven dissipative systems. *Phys. Rev. Lett.* **74**, 2511.

Metcalf, T.R., Jiao, L., McClymont, A.N., Caneld, R.C., Uitenbroek, H.: 1995, Is the solar chromospheric magnetic field force-free? *Astrophys. J.* **439**, 474.

Metcalf, T.R., Leka, K.D., Barnes, G., Lites, B.W., Georgoulis, M.K., Pevtsov, A.A., Balasubramaniam, K.S., Gary, G.A., Jing, J., Li, J., Liu, Y., Wang, H.N., Abramenko, V., Yurchyshyn, V., Moon, Y.-J.: 2006, An overview of existing algorithms for resolving the 180° ambiguity in vector magnetic fields: Quantitative tests with synthetic data. *Solar Phys.* **237**, 267.

Miyagoshi, T., Yokoyama, T.: 2004, Magnetohydrodynamic simulation of solar coronal chromospheric evaporation jets caused by magnetic reconnection associated with magnetic flux emergence. *Astrophys. J.* **614**, 1042.

Moon, Y.-J., Choe, G.S., Yun, H.S., Park, Y.D., Mickey, D.L.: 2002, Force-freeness of solar magnetic fields in the photosphere. *Astrophys. J.* **568**, 422.

Nakagawa, Y., Raadu, M.A.: 1972, On practical representation of the magnetic field. *Solar Phys.* **25**, 127.

Otto, A.: 2001, Geospace Environment Modeling (GEM) magnetic reconnection challenge: MHD and Hall MHD – Constant and current dependent resistivity models. *J. Geophys. Res.* **106**, 3751.

Pandey, B.P., Wardle, M.: 2012, Hall instability of solar flux tubes in the presence of shear flows. *Mon. Not. Roy. Astron. Soc.* **426**, 1436.

Pandey, B.P., Wardle, M.: 2013, Magnetic diffusion driven shear instability of solar flux tubes. *Mon. Not. Roy. Astron. Soc.* **431**, 570.

Petrie, G.J.D., Sudol, J.J.: 2010, Abrupt longitudinal magnetic field changes in flaring active regions. *Astrophys. J.* **724**, 1218.

Petrovay, K.: 1994, Theory of passive magnetic field transport. In: Rutten, R.J., Schrijver, C.J. (eds.) *Solar Surface Magnetism*, Kluwer Academic, Dordrecht, 415.

Potts, H.E., Diver, D.A.: 2009, A repository of precision flat fields for high-resolution MDI continuum data. *Solar Phys.* **258**, 343.

Ravindra, B., Longcope, D.W., Abbett, W.P.: 2008, Inferring photospheric velocity fields using combination of minimum energy fit, local correlation tracking and Doppler velocity. *Astrophys. J.* **677**, 751.

Régnier, S., Priest, E.R.: 2007, Free magnetic energy in solar active regions above the minimum-energy relaxed state. *Astrophys. J. Lett.* **669**, L53.

Sakurai, T., Hagino, M.: 2003, Magnetic helicity of solar active regions and its implications. *J. Korean Astron. Soc.* **36**, 7.

Santos, J.C., Büchner, J., Zhang, H.: 2008, Inferring plasma flow velocities from photospheric vector magnetic field observations for the investigation of flare onsets. *Adv. Space Res.* **42**, 812.

Scherrer, P.H., Bogart, R.S., Bush, R.I., Hoeksema, J.T., Kosovichev, A.G., Schou, J., Rosenberg, W., Springer, L., Tarbell, T.D., Title, A., Wolfson, C.J., Zayer, I., MDI Engineering Team: 1995, The solar oscillations investigation Michelson Doppler imager. *Solar Phys.* **162**, 129.

Schou, J., Scherrer, P.H., Bush, R.I., Wachter, R., Couvidat, S., Rabello-Soares, M.C., Bogart, R.S., Hoeksema, J.T., Liu, Y., Duvall, T.L. Jr., Akin, D.J., Allard, B.A., Miles, J.W., Rairden, R., Shine, R.A., Tarbell, T.D., Title, A.M., Wolfson, C.J., Elmore, D.F., Norton, A.A., Tomczyk, S.: 2012, Design and ground calibration of the helioseismic and magnetic imager (HMI) instrument on the Solar Dynamics Observatory (SDO). *Solar Phys.* **275**, 229.

Schrijver, C.J., Derosa, M.L., Metcalf, T.R., Liu, Y., Mctiernan, J., Régnier, S., Valori, G., Wheatland, M.S., Wiegelmann, T.: 2006, Nonlinear force-free modeling of coronal magnetic fields part I: A quantitative comparison of methods. *Solar Phys.* **235**, 161.

Schuck, P.W.: 2005, Local correlation tracking and the magnetic induction equation. *Astrophys. J. Lett.* **632**, L53.

Schuck, P.W.: 2008, Tracking vector magnetograms with the magnetic induction equation. *Astrophys. J.* **683**, 1134.

Schuck, P.W.: 2010, The photospheric energy and helicity budgets of the flux-injection hypothesis. *Astrophys. J.* **713**, 1.

Seehafer, N., Fuhrmann, M., Valori, G., Kliem, B.: 2007, Force-free magnetic fields in the solar atmosphere. *Astron. Nachr.* **328**, 1166.

Simon, G.W., Weiss, N.O.: 1997, Kinematic modeling of vortices in the solar photosphere. *Astrophys. J.* **489**, 960.

Singh, K.A.P., Shibata, K., Nishizuka, N., Isobe, H.: 2011, Chromospheric anemone jets and magnetic reconnection in partially ionized solar atmosphere. *Phys. Plasmas* **18**, 111210.

Smagorinsky, J.: 1963, General circulation experiments with the primitive equations. *Mon. Weather Rev.* **91**, 99.

Snodgrass, H.B.: 1984, Separation of large-scale photospheric Doppler patterns. *Solar Phys.* **94**, 13.

Snodgrass, H., Ulrich, R.: 1990, Rotation of Doppler features in the solar photosphere. *Astrophys. J.* **351**, 309.

Solanki, S.K., Walther, U., Livingston, W.: 1993, Infrared lines as probes of solar magnetic features: VI. The thermal-magnetic relation and Wilson depression of a sunspot. *Astron. Astrophys.* **277**, 639.

Somov, B.V.: 2007, The Bastille Day 2000 flare. *Plasma Astrophys.* **341**, 468.

Spangler, S.R.: 2009, Joule heating and anomalous resistivity in the solar corona. *Nonlinear Proc. Geophys.* **16**, 443.

Spitzer, L. Jr.: 1962, *Physics of Fully Ionized Gases*, Interscience, New York, 136.

Steffen, M.: 2009, Solar photosphere and chromosphere. In: Trümper, J.E. (ed.) *The Landolt-Börnstein Database*, Springer, Berlin, 39.

Sudol, J.J., Harvey, J.W.: 2005, Longitudinal magnetic field changes accompanying solar flares. *Astrophys. J.* **635**, 647.

Taylor, J.: 1974, Relaxation of toroidal plasma and generation of reverse magnetic fields. *Phys. Rev. Lett.* **33**, 1139.

Theobald, M.L., Fox, P.A., Sofia, S.: 1994, A subgridscale resistivity for magnetohydrodynamics. *Phys. Plasmas* **1**, 3016.

Tikhonov, A.N.: 1963, Solution of incorrectly formulated problems and regularization method. *Sov. Math. Dokl.* **4**, 1035.

Tiwari, S.K.: 2011, Are the photospheric sunspots magnetically force-free in nature? In: Choudhary, D.P., Strassmeier, K.G. (eds.) *The Physics of Sun and Star Spots*, *IAU Symp.* **273**, 1.

Uritsky, V.M., Klimas, A.J.: 2005, Hysteresis-controlled instability waves in a scale-free driven current sheet model. *Nonlinear Proc. Geophys.* **12**, 827.

Veronig, A.M., Karlick, M., Vrsnak, B., Temmer, M., Magdalenic, J., Dennis, B.R., Otruba, W., Pötzi, W.: 2006, X-ray sources and magnetic reconnection in the X3.9 flare of 2003 November 3. *Astron. Astrophys.* **446**, 675.

Vincent, A., Charbonneau, P., Dubé, C.: 2012, Numerical simulation of a solar active region. I: Bastille Day flare. *Solar Phys.* **278**, 367.

Wang, H., Liu, Ch.: 2010, Observational evidence of back reaction on the solar surface associated with coronal magnetic restructuring in solar eruptions. *Astrophys. J. Lett.* **716**, L195.

Welsch, B.T., Fisher, G.H., Abbet, W.P., Regnier, S.: 2004, ILCT: Recovering photospheric velocities from magnetograms by combining the induction equation with local correlation tracking. *Astrophys. J.* **610**, 1148.

Welsch, B.T., Abbett, W.P., DeRosa, M.L., Fisher, G.H., Georgoulis, M.K., Kusano, K., Longcope, D.W., Ravindra, B., Schuck, P.W.: 2007, Tests and comparisons of velocity inversion techniques. *Astrophys. J.* **670**, 1434.

Welsch, B.T., Li, Y., Schuck, P.W., Fisher, G.H.: 2009, What is the relationship between photospheric flow fields and solar flares? *Astrophys. J.* **705**, 821.

Woltjer, L.: 1958, A theorem on force-free magnetic fields. *Proc. Natl. Acad. Sci. USA* **44**, 489.

Wu, S.T., Wang, A.H., Plunkett, S.P., Michels, D.J.: 2000, Evolution of global-scale coronal magnetic field due to magnetic reconnection: The formation of the observed blob motion in the coronal streamer belt. *Astrophys. J.* **545**, 1101.

Zheligovsky, V.A., Podvigina, O.M., Frisch, U.: 2001, Dynamo effect in parity-invariant flow with large and moderate separation of scales. *Geophys. Astrophys. Fluid Dyn.* **95**, 227.